Zimmerli *et al. Swiss Journal of Geosciences* (2024) 117:18
https://doi.org/10.1186/s00015-024-00463-6

SGG SGS sc | nat
Swiss Journal of Geosciences

RESEARCH Open Access

Facies variability and depositional cyclicity in central Northern Switzerland: insights from new Opalinus Clay drill cores

Géraldine N. Zimmerli[1*], Stephan Wohlwend[2], Gaudenz Deplazes[3], Jens Becker[3], Andreas Wetzel[4], Fabio Francescangeli[1] and Anneleen Foubert[1]

Abstract

The Opalinus Clay, a silty to sandy claystone formation, Early to Middle Jurassic (Toarcian and Aalenian) in age, has been selected as the host rock for deep subsurface disposal of radioactive waste in Switzerland. Over the past thirty years, numerous geotechnical, mineralogical, and sedimentological studies have been conducted on the Opalinus Clay within the framework of the Nagra (National Cooperative for the Disposal of Radioactive Waste) deep drilling campaigns and the Mont Terri Project, an international research program dedicated to the study of claystone. The present study aims to unravel the variability of the lateral and vertical facies of the Opalinus Clay in central Northern Switzerland and to place this variability in a regional and basinal context. Analyses of new cores drilled in central Northern Switzerland, including petrographic, mineralogical (X-ray diffraction, multi-mineral interpretation), geochemical (X-ray fluorescence), statistical (non-metric multidimensional scaling analysis), and bedding dip and azimuth data, shed new light on the depositional facies and the spatial and temporal variability of the Opalinus Clay. Petrographic descriptions encompass nine new drill cores using a revised subfacies/facies classification scheme based on texture (colour, grain size, bedding) and composition (mineralogy). Particularly, one new subfacies (SF6) is described and interpreted as mass-wasting deposits. The drill cores are correlated laterally using specific marker horizons. This correlation is achieved by combining thorough facies investigations with lithostratigraphy, biostratigraphy, and chemostratigraphy. Six to seven small coarsening-upward cycles and two long-term coarsening-upward sequences can be interpreted as regressive trends. The observed trends are influenced by the interplay between sediment supply, eustatic sea level change, synsedimentary subsidence, but also the palaeogeographic configuration in an epicontinental sea, provenance and delivery of sediments, current dynamics and climate change. Finally, combined results show that the current dynamics in the Opalinus Clay has been underestimated until now and new depositional models, including the occurrence of drift deposits, are discussed.

Keywords Opalinus Clay, Aalenian, Claystone, Sedimentary facies, Mass-wasting deposits, Cycles

Handling editor: Wilfried Winkler.

*Correspondence:
Géraldine N. Zimmerli
geraldine.zimmerli@unifr.ch
Full list of author information is available at the end of the article

Springer Open

© The Author(s) 2024. **Open Access** This article is licensed under a Creative Commons Attribution 4.0 International License, which permits use, sharing, adaptation, distribution and reproduction in any medium or format, as long as you give appropriate credit to the original author(s) and the source, provide a link to the Creative Commons licence, and indicate if changes were made. The images or other third party material in this article are included in the article's Creative Commons licence, unless indicated otherwise in a credit line to the material. If material is not included in the article's Creative Commons licence and your intended use is not permitted by statutory regulation or exceeds the permitted use, you will need to obtain permission directly from the copyright holder. To view a copy of this licence, visit http://creativecommons.org/licenses/by/4.0/.

1 Introduction

The Opalinus Clay (OPA) is a silty to sandy claystone formation from the Late Toarcian and mainly Early Aalenian ages. In Switzerland, it has been designated as the host rock for deep subsurface disposal of high-, intermediate- and low-level radioactive waste (Nagra, 2002, 2014a). Since the 1990's, the OPA is one of Switzerland's most studied rock formations. Over the last three decades, numerous chemical, biological, mechanical, hydrological, and thermal experiments were implemented in the Mont Terri rock laboratory (Thury & Bossart, 1999; Pearson et al., 2003; Bossart & Thury, 2008; Jaeggi et al., 2014; Bossart et al., 2017; Waber & Rufer, 2017, among others).

OPA appears lithologically uniform at the formation-scale compared to other Mesozoic formations in Northern Switzerland, such as the Staffelegg Formation (Reisdorf et al., 2011) or the Passwang Formation (Burkhalter, 1996; Wohlwend et al., 2019) and its eastern equivalents («Murchisonae-Oolith Formation», Wedelsandstein Formation and «Humphriesioolith Formation»; Bläsi et al., 2013). At higher spatial resolution (m-scale and dm- to cm-scale), considerable lithological variability occurs. Lateral and vertical facies heterogeneities have been observed in OPA, and a subfacies classification scheme has been developed in western Switzerland using several OPA drill cores (Lauper et al., 2018, 2021b) in order to harmonise petrographic descriptions in a standardised, quantitative, and comparative way within all fields of OPA research. Five subfacies are defined and mainly distinguished by texture (i.e., grain size, fabric, colour, sedimentary structures) and composition (i.e., mineralogy; Lauper et al., 2018, 2021b). Subfacies descriptions are critical for assessing and understanding lateral and vertical facies variability on a regional scale. Accurate petrographic descriptions are an important prerequisite for many geotechnical and geochemical studies and predictive modelling of petrophysical properties.

To date, only Mont Terri drill cores in western Switzerland and three cores in central Northern Switzerland such as Riniken (RIN), Weiach(WEI), and Benken (BEN; Lauper et al., 2021b, see Fig. 1B for location) have been analysed concerning the subfacies classification scheme. No basin-wide study has been performed to encompass those facies variations so far. Nagra (National Cooperative of the Disposal of Radioactive Waste) investigated three potential sites (identified as siting regions), where radioactive waste could be stored in OPA: Jura Ost, Nördlich Lägern and Zürich Nordost (Fig. 1B). Two to four new boreholes were drilled at each site: Bözberg-2 (BOZ2) and Bözberg-1 (BOZ1) in Jura Ost, Bachs-1 (BAC1), Stadel-2 (STA2), Stadel-3 (STA3) and Bülach-1 (BUL1) in Nördlich Lägern, Marthalen-1 (MAR1), Rheinau-1 (RHE1) and Trüllikon-1 (TRU1) in Zürich Nordost (Fig. 1B). The boreholes were drilled a few kilometres apart and provided high-quality, fresh and unaltered material allowing detailed facies descriptions. Combining unique core material, exposing sedimentary structures and facies in an unaltered manner, with continuous core logging and borehole data, provides valuable and excellent data and information for detailed sedimentary studies. The unaltered continuous core material can encompass vertical and lateral facies variability during Switzerland's Early to Middle Jurassic at high spatial resolution and to relate it to a global context.

Detailed vertical and lateral facies variability with potential lateral correlation horizons have not been discussed until now in clay mineral-rich successions such as the OPA. Also, the small-scale cycles and their link to potential relative sea level and climate changes influencing sediment deposition were never questioned in detail. The availability of new core material opens the venue to study the lithological variability within the OPA and to upscale regional observations to the basin-scale.

This study aims to address and understand vertical and lateral facies variability within the OPA in central Northern Switzerland. This allows to: (1) revise the lithostratigraphic framework and the correlation at subformation level; (2) define depositional and sedimentary environmental conditions during the Late Toarcian and Early Aalenian in central Northern Switzerland; and (3) up-scale regional facies variations and associated depositional changes at basin-scale (central Europe).

2 Geological setting

During the Early to Middle Jurassic, the OPA accumulated in an epicontinental sea covering central Europe, characterised by relatively shallow water depths (Callomon, 2003; Wetzel & Allia, 2003). Based on sedimentary structures such as ripples, the water depth at deposition is estimated at 20–50 m (Allia, 1996; Wetzel & Allia, 1996, 2003). Regarding palaeolatitudes, Europe was 15° further south than today, and the climate was subtropical to tropical (Etter, 1990; Allia, 1996; Callomon, 2003; Haq, 2018). Lateritic soil formation and related weathering processes dominated continental environments and probably impacted the Fe-cycle within this shallow epicontinental sea (Burkhalter, 1995; Thiry, 2000).

Detailed stable isotope analyses ($\delta^{13}C$, $\delta^{18}O$) of marine benthic and nektonic calcareous fossils, and bulk rock samples at high resolution in recent years, however, refined the climatic and palaeoceanographic interpretations, including the Aalenian (e.g., Dera et al., 2011; Korte et al., 2015; Fantasia et al., 2022). The continuous stable carbon isotope record exhibited distinct excursions, which have the potential to serve for correlation (see

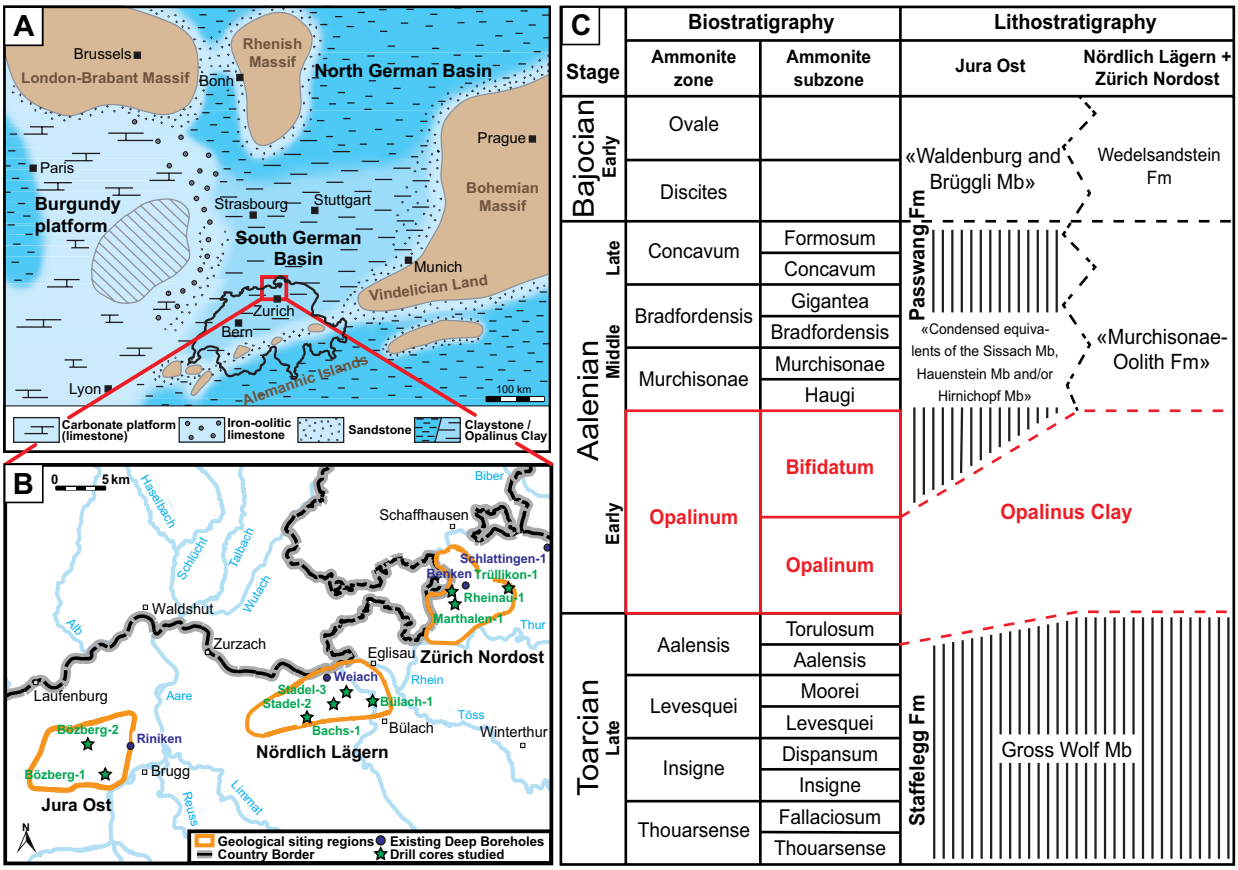

Fig. 1 **A** Palaeogeographic map of the Early Aalenian in central Europe; modified after Nagra (2002) and based on Etter (1990 and references therein) and Wetzel & Allia (2000). Grey hatched area on the Burgundy platform indicates an area with reduced or no sedimentation or intra-Jurassic erosion; possible emerged land mass. **B** Zoom and localisation of the nine studied drill cores (green stars) in the siting regions Jura Ost, Nördlich Lägern, and Zürich Nordost, respectively. The existing deep boreholes are indicated in dark blue. **C** Synthesis of the Late Toarcian, Aalenian, and Early Bajocian biostratigraphy and lithostratigraphy in central Northern Switzerland (Reisdorf et al., 2011; Bläsi et al., 2013; Wohlwend et al., 2019). Dashed lines represent boundaries between the formations. The Opalinus Clay and associated biostratigraphy studied in the framework of this study is marked in red. Hatching: reduced sedimentation and/or condensation. See text for details. *Fm* = Formation, *Mb* = Member

below, Sect. 5.2.2). Furthermore, at the end of the Toarcian, water (surface) temperature dropped by ~ 10 °C although the determined temperature range is wide, showing a decrease from 15–30 °C to 5–15 °C. Colder climatic conditions are therefore assumed for the Aalenian. The climatic conditions affect continental weathering (Ollier, 1969) and, in turn, the delivery of weathering products, including clay minerals to the sea; kaolinite, typical of warm, humid climate, becoming replaced by illite and detrital clay minerals, among others (Ollier, 1969; Blok et al., 2023).

During the Early Jurassic, the opening of the Tethys and the Atlantic Ocean led to a possible reactivation of pre-existing basement structures (Allia, 1996; Wetzel et al., 2003; Reisdorf & Wetzel, 2018), with differential synsedimentary subsidence leading to the fragmentation of the depositional area into local swells and depressions (Allia, 1996; Wetzel & Allia, 2000, 2003; Lauper et al., 2018, 2021b). Overall, the depositional setting is interpreted as a relatively low-energy environment for the clay mineral-rich facies and a high-energy environment for the silty/sandy facies (Lauper et al., 2018, 2021b) with generally high sedimentation rates (Etter, 1990; Leu et al., 2023).

The epicontinental sea was surrounded by landmasses (Vindelician-Bohemian Land to the east, Rhenish Massif to the north, the London-Brabant Massif to the northwest), islands in the south (Alemannic Islands) and a carbonate platform to the west (Burgundy platform, Fig. 1A; Etter, 1990; Allia, 1996; Wetzel & Allia, 2000; Nagra, 2014b; Lauper et al., 2021b). The Swiss Swabian Basin (study area; part of the South German Basin) belonged to the southern part of the Laurasian Seaway. The Laurasian Seaway/Viking Corridor connected the northern margin of the Tethys with the Boreal Arctic Sea

(Bjerrum et al., 2001; Callomon, 2003; Korte et al., 2015). In the south, the Swiss Swabian Basin was connected to the Tethys Ocean via gateways crossing the Alemannic Islands chain.

The OPA has an average thickness of 80–120 m in Northern Switzerland (Nagra, 2002; Wetzel & Allia, 2003), decreasing towards the south. The OPA sedimentary facies consist mainly of sandy to silty claystone with thin, intercalated carbonate-rich horizons. Clay minerals, carbonates, quartz, minor k-feldspar, plagioclase, pyrite, siderite, and mica are abundant minerals. In addition, also 0.1 to 1.5 wt.% of organic carbon is present (Nagra, 2002; Pearson et al., 2003; Bossart & Thury, 2008; Lerouge et al., 2014; Bossart et al., 2017; Mazurek & Aschwanden, 2020). The underlying Staffelegg Formation, the overlying Passwang Formation, and their eastern equivalents are more heterogeneous successions than the OPA. The Staffelegg Formation is dominated by claystone, marl, bituminous units, limestone horizons, and phosphorite-rich strata and was deposited under fully marine conditions (Reisdorf et al., 2011). The Passwang Formation and its eastern equivalents (the boundary is the Swiss Aare River; Bläsi et al., 2013) comprise a series of parasequences dominated by claystone, marl, sandy marl/limestone, bioclastic limestone and iron-oolites (Burkhalter, 1996; Wohlwend et al., 2019; Fig. 1C for lithostratigraphic overview with formations and members).

Figure 1C illustrates the biostratigraphy and lithostratigraphy of the Late Toarcian to Early Bajocian. In addition to the lithostratigraphic units mentioned in Fig. 1C, the Early Toarcian Rietheim Member of the Staffelegg Formation is also considered in this study. In terms of biostratigraphy, the OPA is predominantly represented by a single ammonite subzone known as the Opalinum Subzone from the Opalinum Zone (Dietze et al., 2021; Wohlwend et al., 2021a, 2021b, 2021c, 2022a, 2022b, 2022c, 2022d, 2023a, 2023b, 2024; Fig. 1C). However, the base and the top of the OPA are diachronous, ranging at the base from the upper Aalensis and Torulosum Subzone (Toarcian) to the lower Opalinum Subzone (Aalenian) and in the top from the upper Opalinum to the Bifidatum Subzone (Aalenian; Feist-Burkhardt, 2012; Hostettler et al., 2017, 2020; Lauper, 2021; Lauper et al., 2021a; Wohlwend et al., 2019, 2024; Fig. 1C) as also observed in southwestern Germany (Franz & Nitsch, 2009; Dietze et al., 2021). The duration of the Opalinum Subzone was estimated at 0.6 (Cresta et al., 2001), 0.9 (Leu et al., 2023), 1.0 (Haq et al., 1987; Wetzel & Allia, 2000), 1.8 (Haq, 2018) and 2 Ma (Huang, 2018).

3 Material and methods

For this study, nine new drill cores were studied, and four available drill cores were newly described (Additional file 1). The coordinates of the drill cores, the orientation of the drillings, studied depth horizons, thickness, and references are summarised in Table 1. All studied cores cover the Early Toarcian to Early Bajocian, where the focus of this study is on the Early Aalenian with the Opalinus Clay covering the Opalinum and Bifidatum Subzones (see Fig. 1C; after Reisdorf et al., 2011; Bläsi et al., 2013; Wohlwend et al., 2019).

Table 1 List of all drill cores with abbreviation (abbr.), coordinates (in LV95 and WGS84), orientation of the drillings, studied depth horizon and thickness, as well as references

Drilling name	Abbr.	Coordinates (LV95)	Coordinates (WGS84)	Orientation of drilling	Studied depth horizon (m)	Thickness (m)	References
Bözberg-2	BOZ2	2,652,219/1,261,985	47.50654/8.13174	~⊥ to bedding	445.00–581.91	136.91	Jordan et al. (2022a)
Bözberg-1	BOZ1	2,653,996/1,258,925	47.47888/8.15496	~⊥ to bedding	525.00–659.15	134.15	Schwarz et al. (2022)
Riniken	RIN	2,656,605/1,261,800	47.50452/8.18994	~⊥ to bedding	325.40–459.99	134.59	Matter et al. (1987)
Bachs-1	BAC1	2,674,769/1,264,601	47.52789/8.43148	~⊥ to bedding	791.05–925.49	134.44	Jordan et al. (2023)
Weiach	WEI	2,676,745/1,268,618	47.56379/8.45841	~⊥ to bedding	534.00–678.38	144.38	Matter et al. (1988)
Stadel-2	STA2	2,677,448/1,265,987	47.54004/8.46728	~⊥ to bedding	781.00–916.14	135.14	Jordan et al. (2022b)
Stadel-3	STA3	2,678,793/1,267,162	47.55045/8.48536	~⊥ to bedding	760.00–899.30	139.30	Schürch et al. (2022)
Bülach-1	BUL1	2,681,446/1,266,298	47.54236/8.52044	~⊥ to bedding	878.00–1006.81	128.81	Jordan et al. (2021a)
Marthalen-1	MAR1	2,689,890/1,275,957	47.62812/8.63454	~⊥ to bedding	584.00–721.48	137.48	Jordan et al. (2021b)
Rheinau-1	RHE1	2,689,564/1,277,235	47.63966/8.63046	Oblique to bedding	514.00–687.81	173.81	Schwarz et al. (2023)
Benken	BEN	2,690,990/1,277,843	47.64492/8.64956	~⊥ to bedding	533.00–667.58	134.58	Nagra (2001)
Trüllikon-1	TRU1	2,695,373/1,277,548	47.64165/8.70781	~⊥ to bedding	810.00–944.68	138.68	Schwarz et al. (2021)
Schlattingen-1	SLA1	2,699,381/1,281,630	47.67776/8.76206	~⊥ to bedding	825.00–962.30	137.30	Albert et al. (2012)

Orientation of the drillings: the Mesozoic strata have a dip < 5° (dipping SE). The cores were drilled vertically downwards, which makes almost no difference given the small inclination of the strata

3.1 Petrography

Macroscopic-facies core descriptions are accomplished on nine drill cores ranging in thickness from 128.81 to 142.83 m (BOZ2, BOZ1, BAC1, STA2, STA3, BUL1, MAR1, RHE1, TRU1) and uniquely prepared slabs of three reference cores (BOZ1, BUL1, TRU1; one core per siting region). Cores were drilled approximately perpendicular to the main stratigraphic bedding except RHE1, which was drilled obliquely (173.81 m), representing a true vertical depth of 142.83 m. Slabs were cut from the cores, embedded, and polished to present a clean core surface (Kaehr & Gysi, 2021a, 2021c, 2022a). Slabs constantly expose facies and sedimentary structures, so they provide reference material for the description of the facies and subfacies. High-resolution images (10px/mm, both planar and 360° photographs) also helped to describe facies on slabs and core sections (Kaehr & Gysi, 2021a, 2021b, 2021c, 2022a, 2022b, 2022c, 2022d, 2023; Kaehr et al., 2023). The slabs of the three reference core sections were described and studied in detail using the subfacies classification scheme of Lauper et al. (2018, 2021b). Based on the detailed facies analyses of the three reference cores, the subfacies classification scheme was applied and tested on other cores using both core sections and high-resolution images.

Five subfacies (SF1–SF5) were established for the OPA as the most common lithological end-members observed within the Mont Terri drill cores and three cores from central Northern Switzerland (RIN, WEI, BEN) by Lauper et al. (2018, 2021b). The five subfacies (smallest macroscopically identifiable units) are distinguished by parameters such as lithology, sedimentary structures, and bioclastic content (Fig. 2, macroscopic images). The **argillaceous subfacies 1 (SF1)** is a dark grey, homogeneous, argillaceous, fine mudstone. Dispersed quartz, mica, feldspar grains, and bioclastic fragments occur within the matrix. The **laminated subfacies 2 (SF2)** is an argillaceous-siliceous (siliceous means > 50 wt.% quartz, see Lazar et al., 2015) fine to medium mudstone with lenticular bedding. It shows an alternation of dark grey, argillaceous matrix and continuous to discontinuous, light grey, quartz, and bioclastic-rich lenses (thickness: few mm to few cm). Sparitic Fe-calcite cements most lenses. The **lenticular subfacies 3 (SF3)** consists of a siliceous-argillaceous to siliceous-calcareous medium mudstone. These subfacies have a lenticular to wavy-bedded texture. The lenses are thicker (a few mm to several cm), and the argillaceous matrix contains more quartz grains and bioclastic fragments than SF1 and SF2. The **sandy subfacies 4 (SF4)** is a calcareous-siliceous medium to sandy mudstone. This sandy subfacies (quartz grains and bioclastic fragments) is highly homogenised by bioturbation and shows only a few structures. Clay mineral-rich fractions form discontinuous flaser-like structures. The **bioclastic subfacies 5 (SF5)** is a light grey, homogeneous, silty to sandy bioclastic limestone. Numerous bioclasts up to several mm thick are visible. The remaining fractions are quartz grains, sparitic Fe-calcite cement, or clay minerals. From SF1 to SF5, an evolution from clay-rich over quartz-rich to carbonate-rich can be observed (Lauper et al., 2018). Additionally, lithologies at the interface between two subfacies types can be supplemented with a "+". Thus, SF1+ would represent an SF1 with more lenses than a typical SF1 but not enough for the classification as SF2 (a similar approach to Kneuker & Furche, 2021).

Besides the OPA, the adjacent intervals of the formations below and above were lithologically logged: 7–20 m of the top of the Staffelegg Formation (Rietheim Member and Gross Wolf Member) and 5–20 m of the base of the Passwang Formation («Condensed equivalents of the Sissach Member, Hauenstein Member and/or Hirnichopf Member» and «Waldenburg and Brüggli Member») and its eastern equivalents («Murchisonae-Oolith Formation» and Wedelsandstein Formation). These descriptions allow for a better understanding of the overall depositional conditions. However, mineralogical and geochemical analyses were only performed for the OPA, which is the focus of this study.

3.2 Mineralogy (X-ray diffraction)

Mineralogical compositional analyses (X-ray diffraction; XRD) of the different subfacies were carried out at the University of Bern on bulk samples with measurement intervals of 3 to 5 m for all drill cores except RHE1 (Mäder et al., 2021; Aschwanden et al., 2021, 2022; Gimmi et al., 2022; Wersin et al., 2022; Zwahlen et al., 2022; Gaucher et al., 2023; Mazurek et al., 2021, 2023).

(See figure on next page.)

Fig. 2 Subfacies classification scheme (modified after Lauper et al., 2018, 2021b) with symbolised texture and representative macroscopic picture of the studied subfacies/lithologies (OPA and the bounding units, being Staffelegg Formation, Passwang Formation, and its eastern equivalents). SF1–SF5 correspond to Lauper et al. (2018, 2021b), the newly defined SF6 is shown as two pictures, resp. homogeneous (upper picture) and deformed (lower picture); silty limestone, limestone (micritic/bioclastic) and limestone (iron-rich) are additional lithologies found partly in the OPA; argillaceous marl, calcareous marl and iron-oolites are lithologies in the Staffelegg or Passwang Formations. Scale bar for microfacies: 2 cm for SF1–SF5 and 5 cm for SF6 and onward

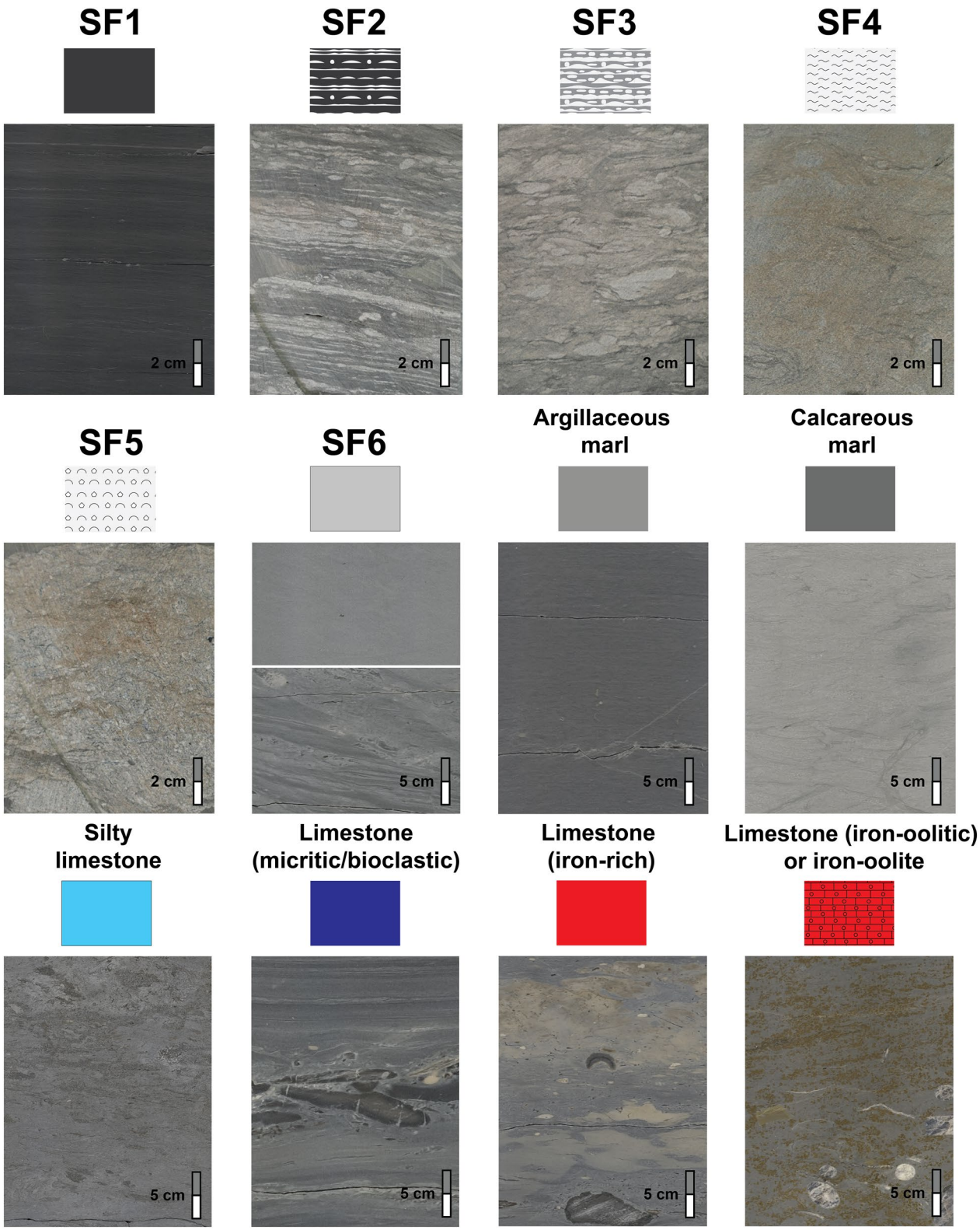

Fig. 2 (See legend on previous page.)

Samples were crushed with a disc mill for a maximum of 30 s. Then, 4 g of rock material was mixed with 1 g of corundum. The mixture and 10 ml ethanol were ground for 6 min (1200 rpm) using a Retsch McCrone XRD-mill. Finally, the powder was dried at 38 °C. All measurements were done using a PANalytical XPertPRO diffractometer. Qualitative analysis was performed using PANalytical HighScore Plus v.4.x and an internal database. Quantitative evaluations were performed using the Rietveld method (Waber, 2020). A total of 346 XRD samples were measured, with 24 to 68 samples measured per core. More measurements were performed for the three reference cores BOZ1, BUL1, and TRU1. The XRD measurements represent the 'typical' OPA facies (representative 'subfacies' types). Clay minerals, quartz, and carbonates are the main constituents of the OPA. Therefore, XRD data have been normalised to 100 wt.% for carbonates (calcite, siderite, dolomite); quartz, k-feldspar, and plagioclase; and clay minerals (kaolinite, illite, smectite, chlorite). According to Füchtbauer (1988) and Naef et al. (2019), the normalised data are presented in a ternary diagram. The XRD results are crucial for understanding and calibrating the XRF (X-ray fluorescence) results (element-mineral correlation).

3.3 Geochemical core logging (X-ray fluorescence)

Geochemical XRF core logging was performed on all nine drill cores at the core facility in Würenlingen (AG). XRF scanning was done with an Olympus Vanta M hand-held XRF analyser mounted on a standard Multi-Sensor Core Logger (MSCL-S) with a logging resolution of 5 cm (Geotek Ltd., UK). The XRF scanner allows measuring the elemental composition of the core surface in a non-destructive manner (Croudace et al., 2019). The instrument was calibrated prior to each measurement. Measurements were performed using an X-ray source (tungsten and rhodium X-ray tube) operating at resp. 40 kV and 10 kV. Count times of 20.00 s were selected for the acquisition of XRF properties. Within the framework of this study, elemental content is used semi-quantitative and relatively using elemental ratios resp. Si/Al and Zr/Al ratios (Ca/Al and Fe/Al ratios are additionally used for statistics).

Aluminium (Al) is of detrital origin (e.g., clay minerals) and is little affected by diagenetic and biological processes such as weathering and redox. Hence, Al has often been used for the normalisation of elemental content (Calvert & Pedersen, 2007; Löwemark et al., 2011). Si/Al indicates quartz (and Al-silicates) over clay mineral content, where the relative change in quartz content may reflect variations in terrigenous sediment supply (Rothwell & Croudace, 2015; Craigie & Rees, 2016). Zirconium (Zr) can be associated with the mineral zircon (heavy mineral; Craigie & Rees, 2016). Si/Al and Zr/Al indicate the presence of detrital grains within the studied regional OPA context (siliciclastic fraction, Lauper et al., 2021a). Moreover, Si/Al and Zr/Al ratios are typically proxies for grain size variations (Calvert & Pedersen, 2007; Craigie & Rees, 2016). Ca/Al is a proxy for all calcite-rich minerals (detrital bioclasts, authigenic and diagenetic carbonates such as cement or concretions) and Fe/Al for Fe-minerals (Rothwell & Croudace, 2015). The iron-rich minerals in the OPA are primarily associated with siderite (or pyrite).

3.4 Multi-mineral interpretation

Multi-mineral interpretation (MM) calculates quasi-continuous curves of mineral content by integrating all available data. Petrophysical downhole logs (caliper log, total gamma-ray, spectral gamma-ray, sonic compressional and shear slowness, resistivity, bulk density, photoelectric factor, neutron hydrogen index, neutron capture cross-section, elemental spectroscopy, nuclear magnetic resonance, spontaneous potential), MSCL data (XRF, bulk density, P wave velocity, magnetic susceptibility, and spectral gamma-ray data) and laboratory measurements from core samples (bulk XRD, total porosity, grain density) were used (e.g., Marnat & Becker, 2020; MM analysis done by Nagra and Ad Terra Energy). Porosity and density were measured on the same plugs as the XRD samples. The multi-mineral interpretation assumes that the measured petrophysical data are a proxy for the specific mineralogy and can, therefore, be used to calculate the mineralogy. Mineralogy is generally assumed, and the theoretical petrophysical data is calculated. By comparing this so-called log response to the actual measured petrophysical data and applying error-minimisation techniques, the mineral content can be deduced even in areas without lab measurements. The more petrophysical data is available, the more precise the calculated mineral content is. On the stacked logs, the following minerals are reported: calcite, siderite, siliciclastics (quartz, k-feldspar, plagioclase), and clay minerals (kaolinite, illite, smectite, chorite). A more in-depth description of the multi-mineral method is given in Marnat & Becker (2020), whereas results for specific boreholes are published in Marnat & Becker (2021a, 2021b, 2021c, 2022a, 2022b, 2022c, 2022d, 2023a, 2023b).

3.5 Non-metric multidimensional scaling

Non-metric multidimensional scaling (NMDS) was performed on elemental content data with input parameters such as Si/Al, Zr/Al, Ca/Al, and Fe/Al. The NMDS was performed to observe and interpret sedimentary trends along the cores. We used NMDS with two dimensions and Bray Curtis distance as a similarity measure. The stress was minimised using a monotone regression (Sibson, 1972). These analyses were only

executed on the three reference cores, where slabs were prepared (BOZ1, BUL1, and TRU1). The R software (R Core Team, 2022) was used with the following packages: "vegan" (to perform multivariate analyses, Oksanen et al., 2016) and "dplyr" (to plot NMDS, Wickham et al., 2022).

3.6 Structural features (bedding and deformation structures)

Dip and dip azimuth of the bedding were measured as part of Nagra's deep drilling campaign. Sedimentary bedding picks were subdivided into 15 bedding types (Ebert et al., 2021a, 2021b, 2021c, 2022a, 2022b, 2022c, 2022d, 2023a, 2023b). For this study, two bedding types were selected; undifferentiated and deformed. Undifferentiated bedding is the planar surface representing the boundary between two different lithological units or internal bedding (undeformed). Deformed bedding is defined when the bedding dip is larger than 15°. The orientation of the bedding was measured on borehole images (planar 360° images) using the software TerraStation II. Rose diagrams showing the dip azimuth were generated for each borehole and each bedding type, resp. the overall undeformed and deformed bedding (SF6 and tilted beds).

4 Results

4.1 Facies analysis

The overall subfacies classification scheme (subfacies and additional lithologies) for the OPA and its bounding units (modified after Lauper et al., 2021b; Fig. 2) was applied to the nine studied drill cores from central Northern Switzerland for lithologic description [Fig. 3 and Additional file 1, including the previously modified drill cores RIN, WEI, BEN (adapted after Lauper et al., 2021b) and Schlattingen-1 (SLA1; see Fig. 1B for location)]. The cores are represented from west to east, and the top of the OPA has been used as a reference level to allow comparison of the OPA descriptions (e.g., Fig. 3): BOZ2 and BOZ1 belong to the westernmost siting region, BAC1 to BUL1 to the middle and MAR1 to TRU1 to the easternmost. The cores show the successions from the Rietheim Member (Staffelegg Formation) to the «Waldenburg and Brüggli Member» (Passwang Formation) and the Wedelsandstein Formation as the eastern equivalent.

The upper two members of the Staffelegg Formation appear uniform and can be correlated laterally. The Rietheim Member consists of argillaceous marl (bituminous) with several micritic limestone beds (three dominant beds in the lower part of the Member, which can be correlated (Wohlwend et al., 2024). The Gross Wolf Member is an argillaceous- to calcareous marl with nodular limestone intercalations. The abundant ammonites in the cores, including several ammonite zones, document a reduced to condensed sedimentation (Wohlwend et al., 2024).

The thickness of the OPA ranges in all nine drill cores from 104.12 to 122.14 m. In Nördlich Lägern the OPA is thinner than in the other two siting regions. For the OPA, SF1, SF2, and SF3 are observed in the nine cores, with SF1 and SF2 being dominant. The sandy SF4 and the bioclastic-rich SF5 are not present in the studied cores, as e.g., defined in Mont Terri (Lauper et al., 2018, 2021b). In the OPA an additional homogeneous or deformed subfacies was identified, which was grouped as the **homogeneous/deformed subfacies (SF6)** (Fig. 3, light grey). Documented only within the OPA, SF6 shows homogenised, folded, or deformed structures and is mainly composed of clay minerals, calcite, and quartz grains. SF6 occurs in SF1- or SF2-dominated units representing a mixture of both subfacies. Because the correlation in Fig. 3 includes not only clay mineral-rich lithologies (OPA), other lithologies were used for the bounding units (classical sedimentary units; after Naef et al., 2019). **Argillaceous marl** (present in Staffelegg Formation and Passwang Formation; middle grey colour in Fig. 3) contains 25–50 wt.% carbonates, 0–25 wt.% quartz and feldspar and 50–75 wt.% clay minerals. **Calcareous marl** (present in Staffelegg Formation and Passwang Formation; dark grey colour in Fig. 3) contains 50–75 wt.% carbonates, 0–25 wt.% quartz and feldspar and 25–50 wt.% clay minerals. **Silty limestone** (present in OPA and Passwang Formation; thickness: 0.07–0.45 m) shows silt to sand-sized quartz grains, with micas, feldspars, bioclastic fragments, clay minerals, pseudosparitic calcite cement and minor pyrite, and is highly bioturbated (indicated in light blue in Fig. 3; Lauper, 2021). These beds resemble SF4 (Lauper, 2021) and have additional pseudosparitic cement. **Limestone (micritic and/or bioclastic)** exists in the Staffelegg Formation, OPA, and Passwang Formation (dark blue colour in Fig. 3). **Limestone (iron-rich)** (OPA and Passwang Formation, red colour in Fig. 3) are calcite and siderite-rich beds (iron-rich), with abundant bioclastic debris, lithoclasts, and few concretions. Lauper et al. (2021b) already described distinct limestone beds, distinguishing between silty limestone and concretionary and/or intraclastic calcareous horizons in the OPA. In this study, these facies have been subdivided into silty limestone, micritic and/or bioclastic limestone, and iron-rich limestone, the latter two being summarised as calcareous beds / condensed beds (modified after Lauper et al., 2021b). Finally, the iron-oolitic lithology (present in Passwang Formation, red colour with an iron-ooid pattern in Fig. 3) is an **iron-oolitic limestone or iron-oolite** (Lauper et al., 2021a). Overall, SF1–SF6 represent clay mineral-dominated facies. In contrast, the argillaceous

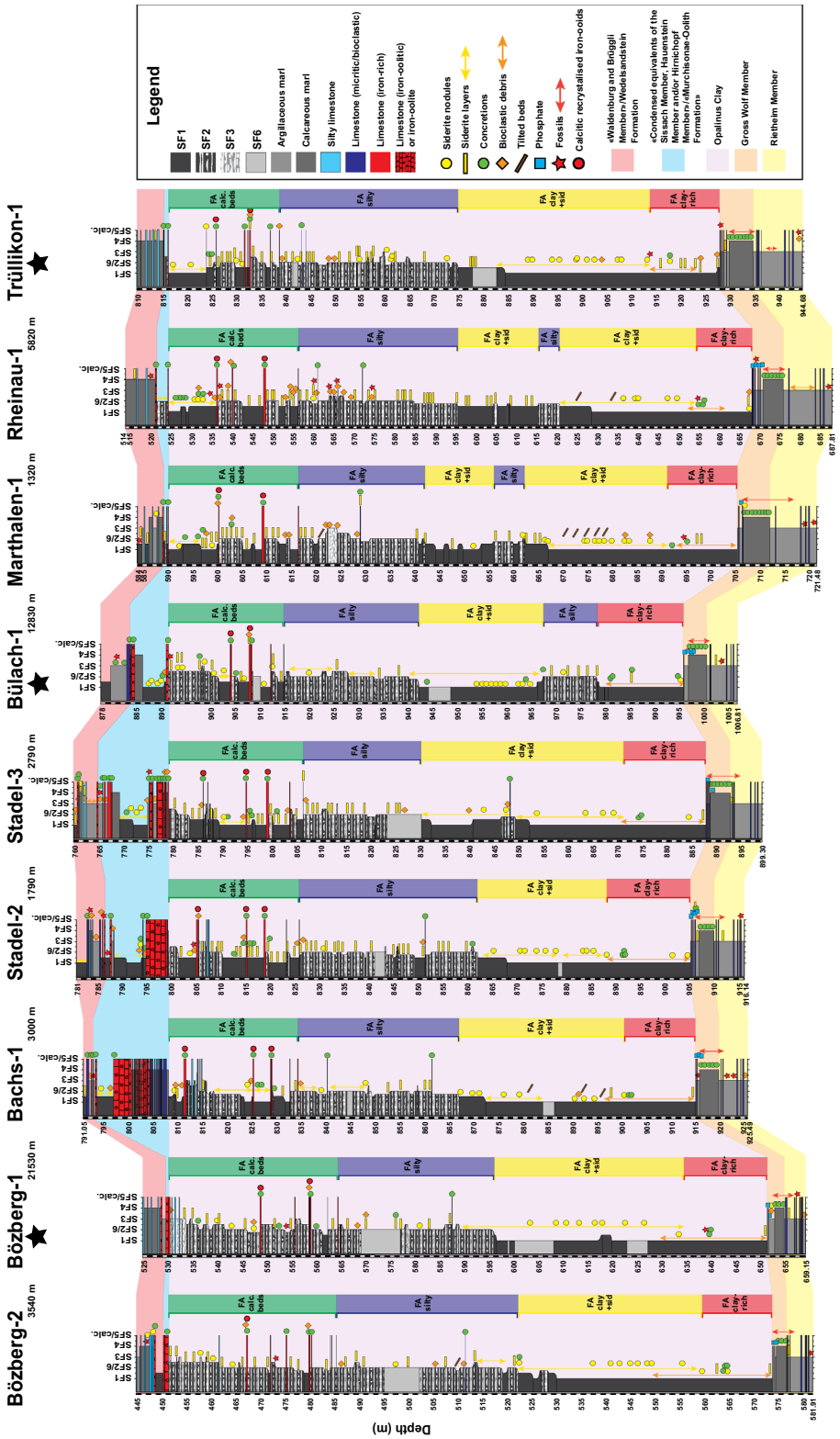

Fig. 3 Overview of the Opalinus Clay succession in the nine drill cores. The RHE1 core has been drilled obliquely but represented here as true vertical depth. Distances between the boreholes are indicated. Main formations, members and the four facies associations within the OPA are indicated. Ten subfacies/lithologies are differentiated in the cores (see legend). Additional attributes such as the presence of siderite nodules, siderite layers, calcareous concretions, bioclastic debris, tilted beds, phosphate traces, fossils, and calcitic recrystalised iron-ooids are visualised by individual symbols at a depth of occurrence (see legend). Reference cores are indicated with stars (cfr. descriptions based on high-quality slabs)

marl, calcareous marl, silty limestone, micritic/bioclastic limestone, iron-rich limestone, and iron-oolitic limestone represent predominantly calcareous facies. The word "SF" (plus a number) was only used for argillaceous facies, for calcareous facies, the lithology is described as text. Additional attributes have been added to complete the detailed facies descriptions of the drill cores, such as the occurrence of siderite nodules/layers (yellow, Fig. 3), calcareous concretions (green, Fig. 3), bioclastic debris (orange, Fig. 3), tilted beds (brown, Fig. 3), phosphate traces (light blue, Fig. 3), fossils (red stars, Fig. 3) and calcitic recrystalised iron-ooids (red circles, Fig. 3). The tilted beds show structures, which are not as pronounced as SF6, but are often related to this subfacies. Tilted beds are mentioned on the lithologs when they are not associated with SF6 but with another SF.

Based on the SF, the OPA can be divided into four main facies associations (FA; Fig. 3), which have to have a minimum thickness of 5 m, namely FA clay-rich (red), FA clay-rich with siderite (yellow), FA silty (blue), FA calcareous beds (green; nomenclature modified after Mazurek & Aschwanden, 2020). In the FA clay-rich within the OPA, only SF1 is present. Calcareous concretions occur in all cores at about 10 m above the base. Only a few siderite layers are visible within this FA. SF1 and SF1+are the dominant subfacies within the FA clay-rich with siderite, but some small SF2 or SF6 intervals are present. Siderite nodules and layers are abundant. In STA3 and BUL1, calcareous concretions (green) and/or micritic/bioclastic limestone are visible. Within the FA silty, SF2 is the dominant facies with minor SF1+, SF3, and SF6 intervals. Thin siderite layers and micritic/bioclastic or iron-rich limestone beds are present. The tilted beds are mostly present in the FA clay-rich with siderite or in the FA silty. Finally, the FA calcareous beds, iron-rich limestone beds are common in the uppermost FA. SF2 and SF3 (with minor SF1+, silty limestone and siderite) are dominant for BOZ2 and BOZ1, from BAC1 to TRU1 SF1, SF1+ and SF2 (with minor SF3, SF6 and silty limestone).

The lower part of the Passwang Formation and its eastern equivalents are rather heterogeneous. For Jura Ost, the base of the Passwang Formation is dominated by iron-oolitic intervals (condensed) followed by an alternation of claystone, argillaceous marl, calcareous marl, and silty limestone beds. Nördlich Lägern shows an alternation of claystone, argillaceous marls, calcareous marls, silty limestone, micritic limestone beds, and iron-oolites and is much thicker than the other cores. Zürich Nordost shows an alternation of claystone, argillaceous marl, calcareous marl, silty limestone beds, and few iron-oolites and is again thinner, similar to Jura Ost (Fig. 3).

4.2 Mineralogy

4.2.1 X-ray diffraction

All XRD measurements and the mean average values per subfacies type for OPA are summarised in Fig. 4A, B. SF1 and SF2 dominate the cores, whereas SF3, SF6, and silty limestone occur subordinately. From SF1 towards silty limestone, there is a clear trend from clay-rich (SF1) towards quartz-rich (SF3) and carbonate-rich (silty limestone). The new macroscopically defined SF6 has a mineralogical composition between SF1 and SF2. SF1, SF6 and SF2 are mineralogically similar.

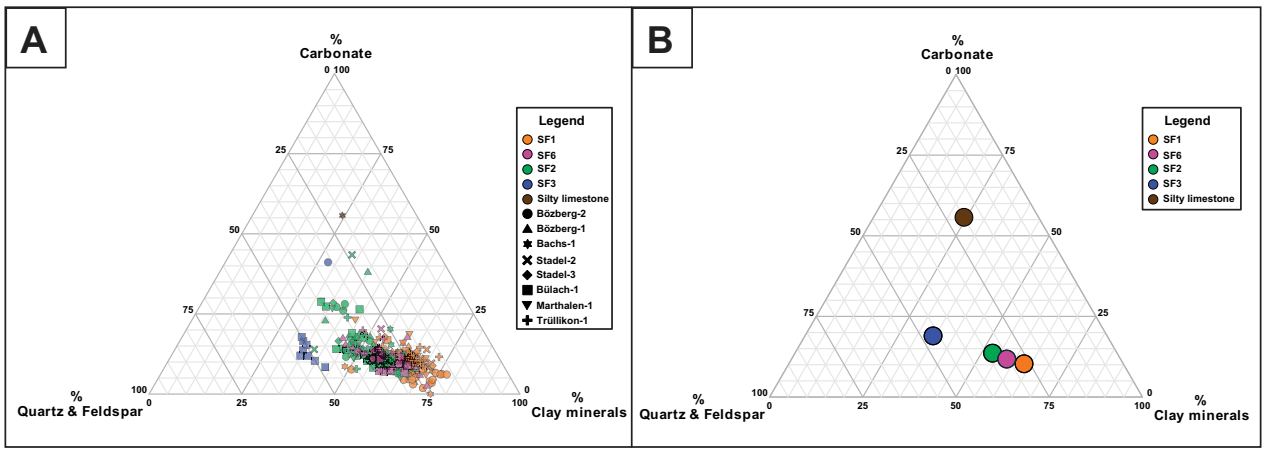

Fig. 4 Mineralogical composition of the subfacies samples within the eight studied drill cores. **A** Mineralogical composition of 346 samples (XRD-data from Uni Bern, Mazurek et al., 2023). **B** Average composition per subfacies. Please note that the limestone beds have not been analysed. The results are represented in a ternary diagram after Füchtbauer (1988), with each corner representing 100 wt.% of resp. clay minerals, quartz and feldspar, and carbonates

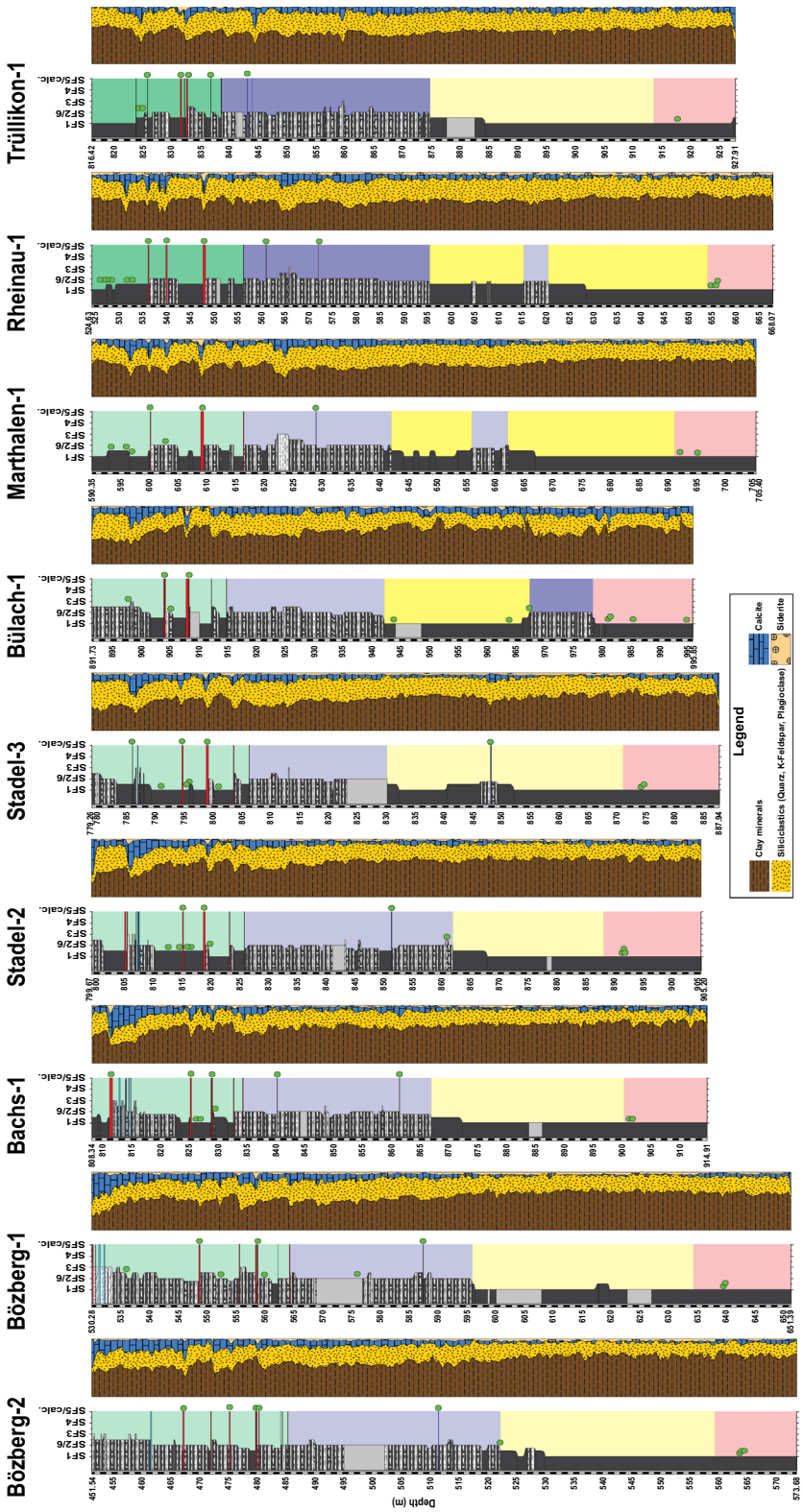

Fig. 5 Multi-mineral interpretation (MM-data, references see text) in stacked log plots for the nine studied drill cores. The mineral contents are in weight percent (wt.%), and the width corresponds to 100 wt.%. Clay minerals are indicated in brown, siliciclastics in yellow, calcite in blue, and siderite in light orange. An offset between core depth and wireline depth of ~ 1 m is noted in STA2, in the other cores, the offset is less. Facies associations (FA) are indicated (red: FA clay-rich, yellow: FA clay-rich with siderite, blue: FA silty, green: FA calcareous beds), as well as calcareous concretions (green)

4.2.2 Multi-mineral interpretation

For the nine drill cores, multi-mineral quantification was normalised to 100 wt.% (Fig. 5). The lower part of the logs (FA clay-rich and FA clay-rich with siderite) consist of ~ 65 wt.% clay minerals and ~ 25–30 wt.% siliciclastics (quartz, k-feldspar, plagioclase). Calcite (detrital and biogenic) and siderite are minor components (~ 7 wt.%). The FA clay-rich area with siderite, is 1 to 3 wt.% higher in siderite content than the FA clay-rich area. Within the FA silty, ~ 30–40 wt.% of siliciclastic minerals are observed. The percentage of clay minerals is ~ 50 wt.%, and calcite increases to ~ 10–15 wt.%. In the uppermost part (FA calcareous beds) of BOZ2 and BOZ1, a trend towards a higher siliciclastic and calcite fraction can be observed (~ 40 wt.% clay minerals, ~ 30–40 wt.% calcite and ~ 20–30 wt.% siliciclastics). In the lower part of the FA calcareous beds in cores BAC1 to BUL1, there is an increased presence of clay minerals, accompanied by reduced amounts of calcite and siliciclastics. The clay mineral content decreases towards the top, and the siliciclastic and calcite content increase. In MAR1 to TRU1, the clay minerals increase, and the siliciclastics and calcite decrease. Concretions, silty limestone, and limestone beds are enriched in calcite and siderite with lower clay and siliciclastic contents (~ 25–30 wt.% calcite, ~ 30–40 wt.% clay minerals, ~ 20–25 wt.% siliciclastics and ~ 5–15 wt.% siderite). The siderite contents are generally low, except in limestone beds, which may contain up to 15 wt.% siderite. Limestone-dominated intervals evidence a significant increase in calcite content.

4.3 Geochemistry

4.3.1 X-ray fluorescence

Overall, Si/Al and Zr/Al ratios show similar variations along the cores (Fig. 6). Higher Si/Al and Zr/Al ratios are detected within the SF2- and SF3-dominated intervals (FA silty), indicating a higher quartz and zircon content, whereas lower values are present within SF1 and SF6 (FA clay-rich and FA clay-rich with siderite; Fig. 6). Some peaks in SF1, may represent quartz-rich units in clay mineral-rich facies. Higher Si/Al and Zr/Al ratios are detected in the FA calcareous beds in BOZ2 and BOZ1 and in the uppermost part of BAC1 to BUL1 due to SF2 and SF3. Lower ratios are present in MAR1 to TRU1 due to the presence of SF1. Moreover, some trends towards higher Si/Al and Zr/Al ratios are visible in the cores (Fig. 6). An increasing upcore trend can be observed, especially within the FA silty and FA calcareous beds. For example, in BAC1, a pronounced trend towards the uppermost limestone bed is evident (Fig. 6). Most of those trends end with the appearance of clay mineral-rich facies (finer lithologies) where the Si/Al and Zr/Al ratios are again decreasing.

4.3.2 Non-metric multidimensional scaling

For the NMDS analyses, the stress values (in all the cases < 0.1) indicate reliable results since the ordination summarises the observed distances among the samples very well (Fig. 7). For BOZ1, the different subfacies/lithologies are progressively displaced along the first axe: SF3, silty limestone, and limestone beds are placed at the left, whereas SF1, SF6, and SF2 mainly at the right of NMDS1 (Fig. 7A). For BUL1, SF2 and limestone beds are placed at the left whereas SF1 and SF6 at the right of NMDS1 (Fig. 7B). For TRU1, SF3 and limestone beds are placed at the right whereas SF1, SF6, and SF2 mainly at the left of NDMS1 (Fig. 7C). SF1, SF6, and SF2 are close together, with SF6 always between SF1 and SF2. SF3, silty limestone, and limestone beds are further apart.

4.4 Bedding and deformation structures

The undifferentiated bedding (green) shows a dip of < 15°, and the deformed bedding (red) a dip normally of > 15°. Undifferentiated bedding shows a consistent southeast dip azimuth across all boreholes (Fig. 8). The uppermost SF6 interval in BOZ2 and BOZ1 (orange, Fig. 8) shows dip azimuth of deformed bedding in north-northeast direction, in STA2 and STA3 (yellow, Fig. 8) in south-southeast direction, the second SF6 bed of BOZ1, BAC1 and STA2 (blue, Fig. 8) in east direction and the tilted beds in MAR1 and RHE1 (green, Fig. 8) in east direction. No correlation of bedding dip azimuth was observed along the other beds.

5 Discussion

5.1 Revised homogenised facies classification for the OPA

5.1.1 Facies and facies associations

The application of the lithofacies classification scheme has many advantages. Approximately 120 m OPA and the upper and lower bounding units, can be compared vertically and laterally over many kilometres. The subfacies classification scheme of Lauper et al. (2018, 2021b) has been adapted for central Northern Switzerland. In the OPA, SF1, SF2, and SF3 still occur, but SF6 has been added to the facies classification scheme, as well as the lithologies silty limestone, micritic/bioclastic limestone, and iron-rich limestone. Those facies have not been observed so far in the Mont Terri region. In addition to the different subfacies/lithologies, four facies associations (FAs) within the OPA were identified. The four FAs were found in the same order in each core with some exceptions of FA silty within the FA clay-rich with siderite for BUL1 to RHE1. The thickness of each FA varies locally from core to core. Moreover, the subfacies distribution aligns well with the previous drillings from the three siting regions: RIN, WEI, BEN, and SLA1 (see Additional file 1 and descriptions by Lauper et al., 2021b).

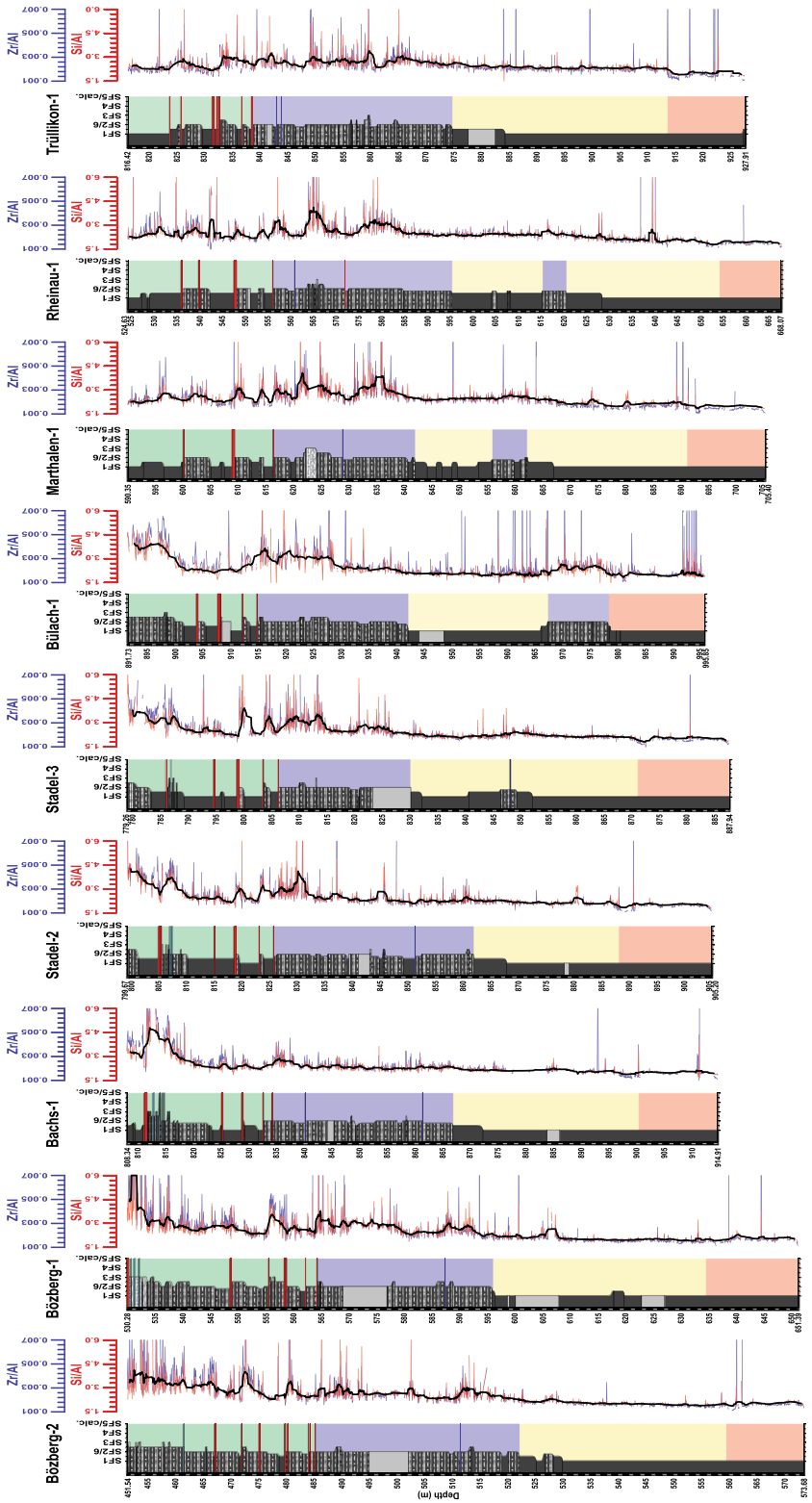

Fig. 6 Subfacies and elemental ratios (XRF-data see references in text; Si/Al in red, Zr/Al in blue, and 1 m moving average of Si/Al in black) for the nine drill cores. Facies associations are indicated (red: FA clay-rich, yellow: FA clay-rich with siderite, blue: FA silty, green: FA calcareous beds)

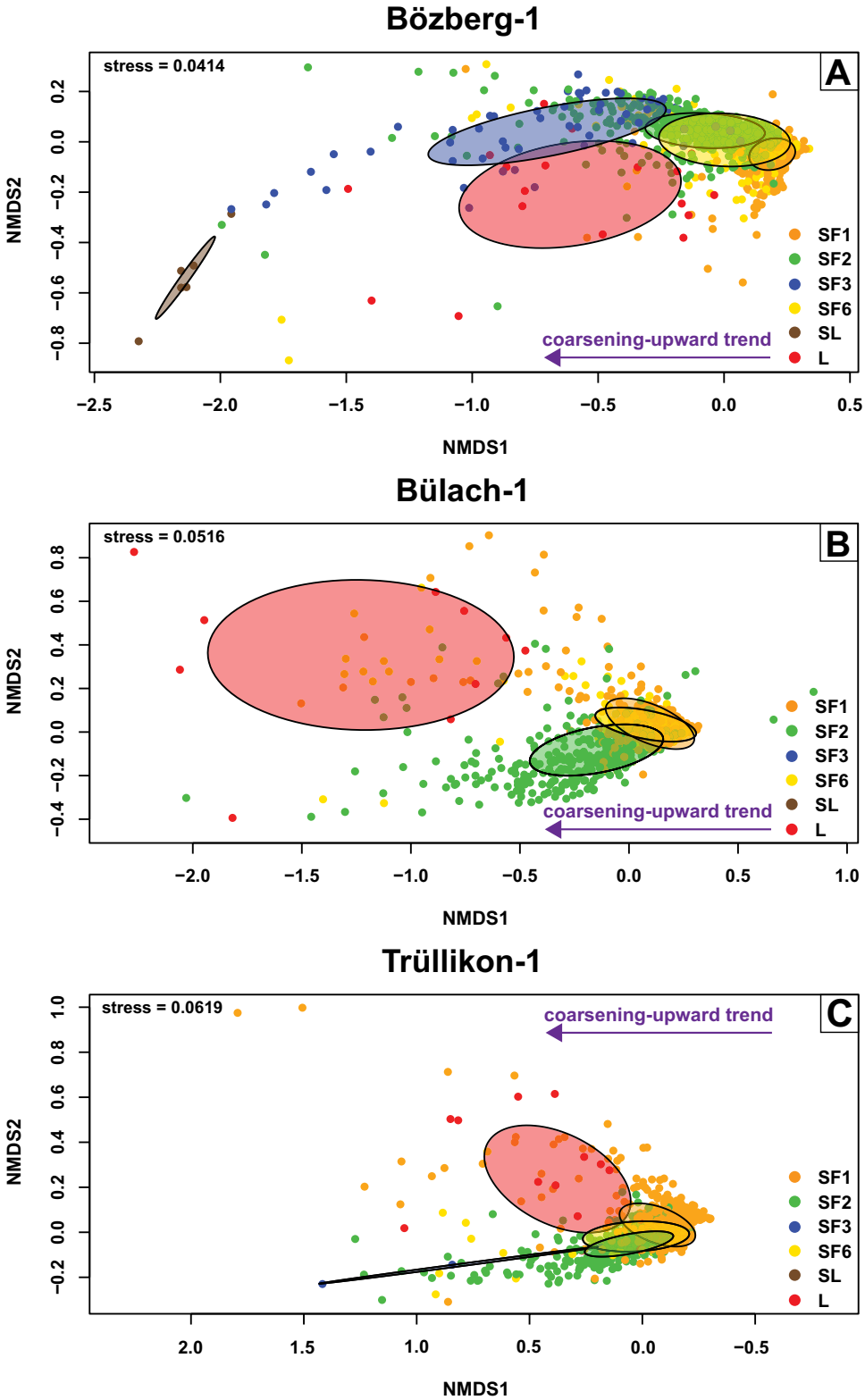

Fig. 7 Non-metric multidimensional scaling analysis of three reference cores BOZ1 (**A**), BUL1 (**B**) and TRU1 (**C**). The six colours represent the six subfacies/lithologies (development from finer to coarser lithologies; SL for silty limestone, L for limestone). The coloured circles show the confidence intervals per subfacies/lithology

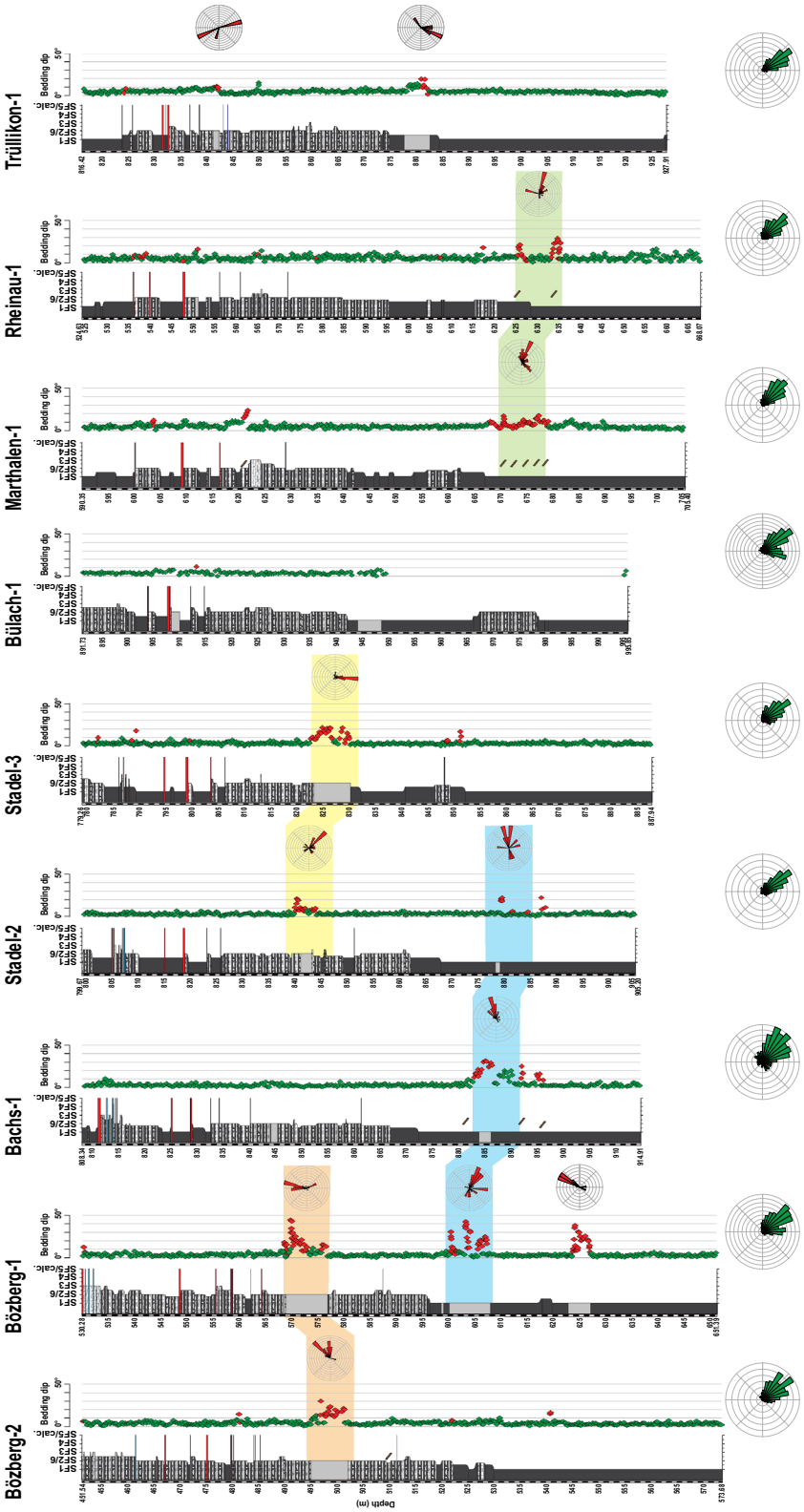

Fig. 8 Undifferentiated bedding and deformed bedding of nine drill cores (data references see text). The bedding dips are illustrated in downcore graphs, and the bedding dip azimuths are shown in rose diagrams. Undifferentiated bedding is shown in green, and deformed bedding in red. Similar bedding dip azimuths of SF6 and tilted beds (in brown) of BOZ2, BOZ1, BAC1, STA2, STA3, MAR1, and RHE1 are highlighted in distinct colours (orange, yellow, blue, and green)

Mineralogical (XRD and MM) and geochemical (XRF) data are appropriate for quantifying the facies variability within the OPA and can be related to the different subfacies/lithologies and facies associations. XRD measurements distinguish all the facies (Fig. 4), evolving from clay-rich to quartz-rich and carbonate-rich from SF1 to silty limestone. Moreover, NMDS analyses evidence that lithofacies can be distinguished statistically using Si/Al, Zr/Al, Ca/Al, and Fe/Al. NMDS analysis (Fig. 7) confirms the overall coarsening-upward trend from SF1 to SF3 for BOZ1, from SF1 to SF2 for BUL1, and from SF1 to SF3 for TRU1 (dependent on the facies present in the cores). SF1, SF6, and SF2 are close because they are mineralogically similar and display only minor lithological variations. SF3 is plotting further and the silty limestone beds even more, showing the more significant lithological variations between these facies. SF6 systematically clusters SF1 and SF2, evidencing a mixture between both subfacies. The coarsening-upward trend in Fig. 7 is represented by the elemental ratios reflecting grain size (Si/Al). It can be associated with an increase in quartz and carbonate content and, hence, a change in mineralogy (see XRD). Silty limestone is mineralogically similar to SF4 (Lauper, 2021). The limestone beds (L, red in Fig. 7) show a heterogeneous distribution representing complex diagenesis. The NMDS analysis confirms the use of XRF within these cores. With MM and XRF the subfacies/lithologies are more challenging to distinguish, but the FA could be differentiated. The FA clay-rich and the FA clay-rich with siderite show more clay minerals and lower Si/Al and Zr/Al ratios, with SF1 and SF2 dominating. In contrast, the FA silty shows more siliciclastics and carbonates and higher Si/Al and Zr/Al ratios, with SF2 and SF3 dominating. For the FA calcareous beds, there is a trend from west to east from coarser lithologies for BOZ2 (SF2 and SF3) towards finer ones in TRU1 (SF1), which is observed in the MM and XRF measurements. SF6 is difficult to define by MM and XRF as it is a mineralogical mixture of SF1 and SF2. A combination of XRD, XRF, MM, and NMDS shows that this facies classification is appropriate for these cores.

SF4 and SF5 are not identified in central Northern Switzerland but are dominant in the drill cores from Mont Terri (western Switzerland; Lauper et al. 2018, 2021b). Overall, the five subfacies defined by Lauper et al. (2018, 2021b), together with the additional subfacies SF6 and the additional lithologies (silty limestone, micritic/bioclastic limestone, iron-rich limestone), allow the facies model to be applied to the entire OPA in Switzerland as well as the Opalinuston Formation and the Achdorf Formation in Germany and have many potentials to be applied in other clay-dominated environments. Within this study, three additional lithofacies (argillaceous marl, calcareous marl, iron-oolites) were defined to describe the lower and upper bounding units (top of the Staffelegg Formation and the base of the Passwang Formation and its eastern equivalents).

5.1.2 Mass-wasting deposits in the OPA

SF6 (homogenised/deformed subfacies) has never been described in the OPA cores, except in RIN at 415.90–416.75 m (Matter et al., 1987). Moreover, Kneuker & Furche (2021) mentioned that the chaotic or disrupted bedding in the OPA could result from early sedimentary landslides (slumping). The SF6 beds affect the thickness variations and correlation potential between the drill cores. The layers are homogenised, partly folded, deformed, and show sharp boundaries. The tilted beds (in brown in Fig. 3 and Additional file 1) can be associated with SF6, and the initial facies are still visible.

These layers can be interpreted as mass-wasting deposits. Mass-wasting events refer to sediments' gravitational movement involving failure, dislodgement, liquefaction, and remobilisation (Lewis, 1971; Strachan, 2002; Shanmugam, 2019). When shear stresses exceed the shear strength of the sediments due to factors such as increased or fluctuating pore pressure, overburden pressure caused by sedimentation or erosion, relative sea level fluctuations, wave action (e.g., storms), tectonic loading, slope steepening, earthquakes (in such cases referred to as seismite), fluid seepage, high biological productivity and/or gravity, sediments can be set in motion (Reading, 1996; Montenat et al., 2007; Clarke et al., 2012; Wetzel & Unverricht, 2013; Huhn et al., 2019; Scarselli et al., 2019; Alsop & Weinberger, 2020). Complex internal deformation can occur as sediment moves downslope, including plastic deformation, but remnants of original bedding may still be preserved (Reading, 1996). Mass-wasting deposits can occur on low-gradient slopes with high sedimentation rates (Reading, 1996). Earthquake-induced liquefaction and sediment flow have been documented on slopes with gentle gradients, ranging from 0.25° (Field et al., 1982), to less than 1° (García-Tortosa et al., 2011; Gibert et al., 2011) and 1–4° (Lewis, 1971). Slope conditions in the OPA basin are likely similar to these conditions.

Several case studies have provided support for investigating the mass-wasting deposit hypothesis. A homogenite triggered by a tsunami was described in the Ionian Sea in the Mediterranean (Hieke, 1984; Hieke & Werner, 2000) and a megaturbidite in the central South China Sea (Wetzel & Unverricht, 2013). Moreover, soft-sediment deformation/disturbance or completely homogenised sediment triggered by an earthquake (Owen & Moretti, 2011) is documented in lakes in Chile (Molenaar et al., 2022) and lakes in the Swiss Alps (Schnellmann et al., 2002, 2005, 2006; Kremer et al., 2017; Strupler et al.,

2018; Nigg et al., 2021; Bellwald et al., 2024). Homogenised beds and slow deformation structures are also described in Paganzo Basin (Argentina) as slumping or creeping (Buso et al., 2019). Those deformed and homogenised beds have similarities to the structures found in the OPA.

The homogenised SF6 units in the OPA can result from liquefaction, a gravitational phenomenon often associated with mass-wasting deposits. Fine-grained silt- and mudstone, containing a significant volume of water, are among the most vulnerable sediments (Montenat et al., 2007). When these sediments liquefy during calm conditions (reduction of currents), homogenites can form. If the cohesive sediment is transported as a package, it can be plastically deformed during movement. Both sediment structures (homogenised and folded) are clearly indicative of mass-wasting deposits. The exact trigger for these potential mass-wasting deposits remains uncertain.

The orientation of SF6/tilted beds were determined (Fig. 8). In BOZ1, BOZ2, BAC1, STA2, STA3, MAR1, and RHE1, some SF6/tilted beds could be correlated (see a potential correlation of the beds in orange, yellow, blue and green in Fig. 8) based on the same directions of the deformed beds. The lower SF6/tilted beds have a direction towards the east (in blue and green, Fig. 8), and the upper beds show a direction towards north-northeast for BOZ2 and BOZ1 (in orange, Fig. 8) and towards south-southeast for STA2 and STA3 (in yellow, Fig. 8). There is a general trend towards the east. In BOZ1, BUL1, and TRU1, the descriptions of the facies were based on cores and slabs, which explains why more SF6/tilted beds were observed in these cores. The tilted beds in RIN (Additional file 1; 413.30–416.34 m) could be linked to the blue and SF6/tilted beds in BEN (Additional file 1; 620.00–622.00 m) to the green correlation. Most mass-wasting deposits can be correlated within one siting region (local scale; exception: blue correlation in Fig. 8). However, a simultaneous mass-wasting deposit event within all the nine cores could not be identified (across the three siting regions at regional scale). The maximum distance over which mass-wasting deposits could be correlated is 25 km (blue correlation in Fig. 8). Given the irregular distribution of SF6 within the cores, very localised events may have occurred that cannot be correlated on a regional scale. There are more SF6 beds in the western cores compared to the eastern cores. A deepening of the basin towards the west could be the reason for the uneven distribution of SF6, where conditions became more unstable, resulting in mass-wasting deposits. The similar location of some SF6/tilted beds in neighbouring cores at a very local scale and similar deformed bedding directions is a strong argument for the occurrence of mass-wasting deposits in the OPA.

5.1.3 From facies classification to depositional environment

The depositional model for the OPA has been the subject of debate since the 1990's. Many descriptions and interpretations have been presented, but no comprehensive depositional scenario exists for the OPA at the basin- or regional scale. Most authors described the OPA as tempestite deposits with a distinction between proximal and distal tempestites based on coarser and finer lithologies (Allia, 1996; Wetzel & Allia, 2003; Lauper et al., 2018, 2021b). The OPA can be described as deposited in a storm wave-dominated regime (after Bohacs et al., 2014). During storm events, coarser continental detritus or locally reworked bioclastic material is incorporated in the sediments (Wetzel & Allia, 2003; Wetzel & Meyer, 2006; Lauper et al., 2018, 2021b).

Based on the descriptions of the detailed subfacies/lithologies, other depositional models cannot be excluded. Following Bohacs et al. (2014), three facies association successions may exist: a storm-wave-dominated shelf regime, a river-flood-dominated shelf regime, and a tidal-current-dominated shelf regime. For a river-dominated depositional environment, Wetzel & Allia (1996) already postulated that the OPA sediments were derived from river discharge directly or indirectly, after interim deposition, to their final depositional site. Proximal and distal deposits can explain coarser and finer lithologies. Tidal-current-dominated shelf regimes are characterised by lenticular, cross-bedding, wavy, and flaser beds. Tidal rise and fall produce an alternation of sand (current ripples) and mud present in the OPA (Reading, 1996). In addition to the depositional models of Bohacs et al. (2014), turbidites and drift deposits/contourites can also produce similar lithologies. Turbidites, which have been described as downslope density currents (Rebesco et al., 2014; Shanmugam, 2017; Stow & Smillie, 2020), are event beds and can show cross-laminations, planar laminations, and homogenised fine-grained sediments similar to those found in the OPA. Finally, contourites/drift deposits are sediments deposited or reworked by the action along slope bottom currents (Rebesco et al., 2014; Shanmugam, 2017; Stow & Smillie, 2020). Contourites can be deposited in shallow marginal basins such as the OPA and not only in deep oceans (Rebesco et al., 2014). Contourites are primarily fine-grained and can be composed of mud, silt, and fine sand, depending on the bottom-current intensity (Reading, 1996). Homogeneous, structureless, bioturbated sediments, cross-lamination, flaser and lenticular bedding, lenses, starved ripples, and parallel lamination (Reading, 1996; Wetzel et al., 2008; Rebesco et al., 2014; Shanmugam, 2017; Stow & Smillie, 2020) are typical for contourite deposits, but the same structures can be found in turbidite deposits.

The hemipelagic Early Jurassic Laurasian Seaway of Pliensbachian age (Cardigan Bay Basin, UK; Pieńkowski et al., 2021) and the Upper Jurassic/Lower Cretaceous Vaca Muerta Formation in the Neuquén Basin (Argentina; Paz et al., 2022) have been described as predominantly influenced by contour current transport. The lithology is similar to the OPA. Basin deposits are clay mineral-rich lithologies similar to SF1 and contourite drift deposits similar to SF2 and SF3. Ripples or parallel silt laminae are described as a product of traction transport due to bottom current activity. Thicker ripples have been associated with higher energy currents (Paz et al., 2022).

It is important to consider that various depositional models are possible when dealing with mud sediments in an epicontinental sea. Finally, these sediments may also be transported by processes such as hypopycnal river plumes, hyperpycnal fluvial discharge, and sediment remobilisation due to relative sea level changes (Reading, 1996; Schieber, 2016). Hence, it is conceivable that a combination of different models may be required to explain the deposition of the OPA.

Overall, results indicate that the influence of current dynamics in the Aalenian epicontinental basin has been clearly underestimated in previous studies. The clay- to silt-rich units in the OPA could be the effect of continuous hydrodynamic action resulting in drift deposits. Current studies are focusing on the thorough understanding of grain size variations in the OPA and the reconstruction of past current dynamics. This will certainly shed new light on the depositional conditions and the potential influence of currents within the epicontinental sea covering central Europe during the Aalenian.

5.2 Lateral facies correlation

5.2.1 Facies associations and marker beds

Despite some differences in thickness, the four main FA can be consistently observed in all the cores. At one siting region (local scale), such as Jura Ost, Nördlich Lägern, and Zürich Nordost, there is relatively limited lateral variation in the distribution of the different facies. The FA clay-rich (red shaded area in Fig. 9) exhibits good correlation potential. Its thickness remains relatively consistent across all the cores. In the FA clay-rich with siderite and the FA silty (yellow and blue shaded areas in Fig. 9), lateral variations in the thickness of SF1, SF2, and SF3 packages are observed. However, the overall evolution from SF1 in the FA clay-rich with siderite towards SF2 for the FA silty is similar for all cores. In some cores, SF2 packages (FA silty) appear within the FA clay-rich with siderite, such as in BUL1, MAR1, and RHE1 (Figs. 3, 9 and Additional file 1). This lateral variation can be explained by local changes in water depth (different sub-basins, shallowing towards the east) or shorter distances to a terrigenous source. In the uppermost part of the cores, significant lateral differences in subfacies are observed amongst the drill cores, particularly in OPA's upper part, from the presence of SF3 in BOZ1 to mainly SF1 in TRU1 (Figs. 3, 9, FA calcareous beds). Moreover, a high presence of calcareous beds is visible in every core.

Establishing a lateral correlation between the different sites is challenging. The variability in facies can primarily be attributed to small-scale regional variations in depositional, environmental, and diagenetic conditions. Factors such as synsedimentary tectonics, resulting in differential basins with swells and depressions, probably have played a role in influencing sedimentation patterns (Allia, 1996; Wetzel & Allia, 2003; Wetzel et al., 2003). Moreover, changes in bottom current patterns, sedimentation rate, or sand influx have significantly impacted lateral thickness variations. Given these differences, lateral correlation becomes difficult. Unfortunately, the lower and middle part of the OPA is deposited mostly in the Opalinum Subzone and biostratigraphy does not allow to refine the correlation.

The sideritic/micritic nodules are probably formed due to early diagenetic processes close to the sediment–water interface in suboxic conditions (Wetzel & Allia, 2000; Lauper et al., 2021a). The calcareous beds towards the top of the Opalinus Clay are condensed, thin sediment layers that form during longer periods with reduced sedimentation rates (Föllmi, 2016). These beds are probably formed due to synsedimentary lithification at the seafloor associated with sediment starvation (Lauper et al., 2021a). Although those horizons are diagenetically overprinted,

(See figure on next page.)

Fig. 9 Coarsening-upward cycles within the OPA in the nine studied drill cores are indicated with red triangles. Si/Al ratios are presented next to the lithology. Coarsening-upward cycles are defined by a transition from SF1–SF2 and/or an increase in Si/Al ratios. Two small-scaled coarsening-upward cycles in the lower part and four to five cycles in the upper part are present in each core, and two overall sequences (long-term). The correlative marker beds are indicated in different colours (Bed-I in purple, Bed-II in grey, Bed-IIIa and b in blue, Bed-IV in red, Bed-V in green and Bed-VI in orange). The stratigraphic framework based on combined lithostratigraphy, biostratigraphy, and sequence stratigraphy is presented, as well as their link with marker beds and coarsening-upward cycles. Facies associations are indicated (red for FA clay-rich, yellow for FA clay-rich with siderite, blue for FA silty, and green for FA calcareous beds). *S. Fm.* = Staffelegg Formation, *UBU* = upper bounding unit, Passwang Formation, and eastern equivalents; after Lauper et al. (2021a)

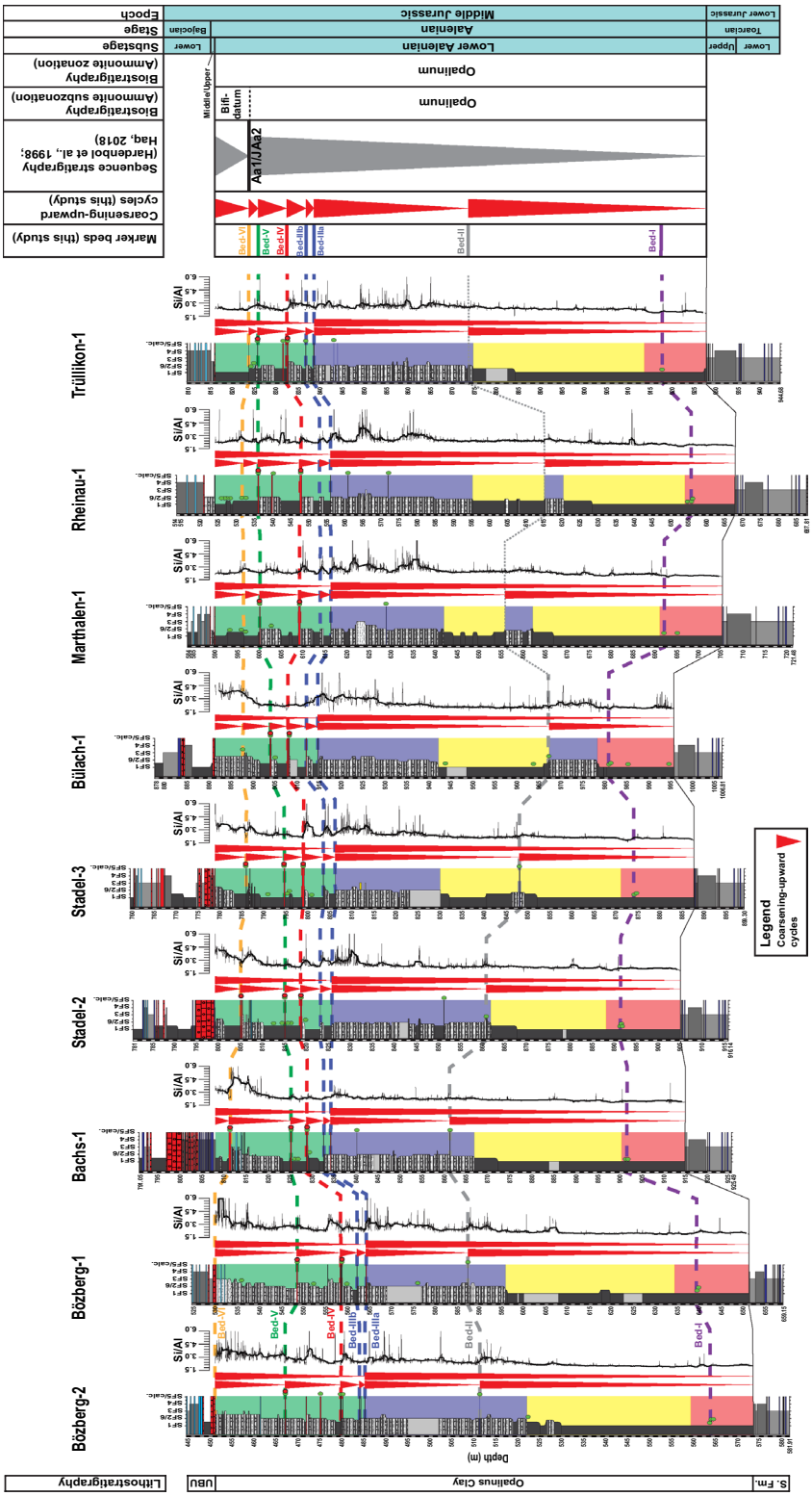

Fig. 9 (See legend on previous page.)

those beds are observed in all studied core sections at similar depths, representing specific deposition conditions within the Aalenian epicontinental sea.

In total, six major calcareous beds are observed in the OPA (Bed-I to VI) and can be used as marker beds (Fig. 9 and Wohlwend et al., 2024).

Bed-I (purple line in Fig. 9): This bed contains calcareous concretions and is located in all studied cores at ~ 10 m above the base of the OPA. Macroscopic observations of these early diagenetic concretions suggest that they are not deformed or transported.

Bed-II (grey line in Fig. 9): This bed is a nodular, bioclastic limestone (fossil-rich with bivalves, echinoderms). The bed is present from BOZ2 to BUL1 and appears in the first SF2 package in the OPA. In STA2 there are two potential calcareous beds (852 and 861 m depth, Fig. 9). The lower bed has been chosen as Bed-II due to the increase in Si/Al ratios. In MAR1, RHE1, and TRU1, this nodular and biomicritic layer is not present (thin and dotted line in Fig. 9). For MAR1 to TRU1 those SF2 packages are present, but probably small-scaled diagenetic conditions changed and thus no calcareous beds could form.

Bed-IIIa and b (blue line in Fig. 9): Those calcareous beds are the lowest most in the FA calcareous beds and look very similar. Those are bioclastic-rich limestone layers (biomicrite) with a lot of bivalves and echinoderms and contain some micrite nodules. Moreover, this horizon is marked by the presence of siderite.

Bed-IV (red line in Fig. 9): This bed is a siderite-rich and fossil-rich calcareous bed with two to four individual beds forming one big correlation horizon. Those beds contain calcitic recrystallised iron-ooids, biomicritic intraclasts, and sometimes nodules.

Bed-V (green line in Fig. 9): This bed is calcareous, nodular, bioclastic-rich, and iron-rich (slightly sideritic and pyritic). The bed contains calcitic recrystallised iron-ooids and many bored nodules and intraclasts.

Bed-VI (orange line in Fig. 9): The uppermost marker bed is the most significant bed. In BOZ2 and BOZ1 this bed is not present and condensed at the top of the OPA (the transition towards the Passwang Formation; contains iron-ooids, intraclasts, and bioclasts). In BAC1, STA2, and STA3 this bed contains iron-ooids (partially replaced by calcite), bioclastic fragments, and have an iron-rich (siderite) and calcite-rich matrix. In BUL1, MAR1, RHE1, and TRU1 this bed is nodular and/or an iron-rich horizon of small thickness.

It should be noted that the identified marker beds can be well correlated at the local scale (within the three sites) due to similar lithological characteristics. The marker beds can therefore be used as correlation horizons. Other calcareous beds are observed in some of the core sections but are only very local due to differing depositional and diagenetic conditions; e.g., see additional calcareous beds in BOZ2, BOZ1, and RHE1 (Fig. 9).

5.2.2 Marker beds as timeline

Although the marker beds can be correlated at local scale, they are mainly based on specific lithological characteristics. Apart from the uppermost calcareous bed (Bed-VI), there is no detailed biostratigraphic or chemostratigraphic support and thus the question arises as to what extent they represent timelines. Also, it is not clear how much time is represented within one marker bed.

However, the lowermost marker bed (Bed-I, Fig. 9) aligns well with the carbon isotope chemostratigraphy suggested by Wohlwend et al. (2024). Wohlwend et al. (2024) mention a negative C-isotope excursion (nCIE) from the organic matter as well as from the inorganic carbonate fraction aligning with this correlation bed, followed by a recovery phase, which may correlate with similar negative carbon isotope excursions during the earliest Aalenian from different locations [Morettini et al., 2002 (Italy); Sandoval et al., 2008 (Spain); Price, 2010 (Scotland); Fantasia et al., 2022 (France and Chile)]. Unfortunately, the biostratigraphy does not allow to constrain this correlation line, as most of the OPA is deposited in the Opalinum Subzone.

The uppermost marker bed (Bed-VI, orange line in Fig. 9) fits very well with biostratigraphy, chemostratigraphy and sequence stratigraphy. This marker bed can be correlated with a significant positive C-isotopic excursion (pCIE) in the drill cores BAC1 to TRU1 which was dated by ammonites to the slightly younger Bifidatum Subzone of the Opalinum Zone (Wohlwend et al., 2024; see also Fig. 1C and 9). However, in BOZ2 and BOZ1, these beds are not present which could be explained by condensation in the Bifidatum Subzone at the top of the OPA. This positive excursion corresponds to pCIE in other time-equivalent records, such as in Spain (Sandoval et al., 2008), in Scotland (Price, 2010), and in France and Chile (Fantasia et al., 2022). Therefore, a global event can be assumed. Stable carbon isotope data from both hemispheres provide evidence of global environmental perturbations in this period (Fantasia et al., 2022). Some of those global signals are probably visible in the CIE registered in the OPA (Wohlwend et al., 2024) and expressed in the formation of the calcareous beds. Although the origin of the calcareous concretions, siderite occurrence, and calcareous beds remain to be studied, their enigmatic origin is potentially related to early diagenetic processes during environmental perturbation.

Additionally, marker Bed-VI (orange line, Fig. 9) can be correlated with the coarsening-upward trends observed by Bläsi (1987), who interpreted that the uppermost trend in RIN corresponds with the top of the OPA

(condensation, as BOZ2 and BOZ1) and in WEI with the top of the uppermost bed (as in all the other cores in Nördlich Lägern). Similar observations in this study confirm this hypothesis. At global scale, Bed-VI may be interpreted as the major sequence boundary Aa1 (European basin study) described by Hardenbol et al. (1998) and JAa2 (global approach) described by Haq (2018; see Fig. 9). Hardenbol et al. (1998) and Haq (2018) determined this sequence boundary as the top lowstand in an overall regressive trend representing sea level fall, followed by a transgression. The sequence boundary Aa1 is located in the middle of the Bifidatum Subzone of the Opalinum Zone (Hardenbol et al., 1998) and JAa2 as about 3/4th up in the Opalinum Zone (Haq, 2018).

Overall, Bed-VI can be interpreted as an important sequence boundary identified by Hardenbol et al. (1998) and Haq (2018), and lines up with the biostratigraphy and chemostratigraphy (e.g., Wohlwend et al., 2024). As such, this bed is interpreted as a timeline (Fig. 9), and as such the most important correlation bed in the OPA. For the other marker beds more biostratigraphic and chemostratigraphic approaches are needed to define them as potential timelines.

5.3 Facies variability through space and time: from cycles to sequences?

5.3.1 From small-scale variations towards coarsening-upward cycles

Small-scale coarsening-upward trends (dm- to m-scale) are present in all cores (red triangles in Fig. 9). They are defined by a transition from SF1 to SF2 and/or an increase in Si/Al ratios (grain size; Figs. 9, 10). Si/Al (grain size) and Zr/Al ratios (more dense material) show similar trends. Figures 10A, B highlight that several coarsening-upward trends are visible at a small scale and stacked on each other. Sometimes, the increase in Si/Al or Zr/Al is less clear, but this can be explained by logging resolution. The coarsening-upward cycles are often covered by limestone beds and/or a layer rich in calcareous concretions (f.e., see Figs. 3 and 9).

The relatively high values in Si/Al and Zr/Al at the end of each cycle (interpreted to trace grain size) could result from a sedimentation break, e.g., due to reduced sediment supply or erosion at the seafloor. They are referred to as "hiatus beds" by Wetzel & Allia (2000), following the idea of "hiatus concretions" by Voigt (1968). Lauper et al. (2021a) suggest sediment bypassing. This can locally result in the enrichment of coarse-grained heavy minerals such as zircon, often coinciding with the top of the calcareous beds and emphasised in the Zr/Al peaks (Fig. 10; also seen in Lauper, 2021; Lauper et al., 2021a). Often, this happens when the sediment deposition is equal to sediment erosion. This process is mainly induced by increased bottom-water energy, low relative sea level, and low sedimentation rates (Burkhalter, 1995; Wetzel & Allia, 2000; Lauper et al., 2021a). Those conditions also steer early diagenetic processes in the shallow subsurface, which may explain the occurrence of calcareous beds and/or calcareous concretions towards the top of each trend.

Six to seven small-scaled coarsening-upward cycles exist in the OPA, in the lower part two and in the upper part four to five (in the FA calcareous beds, see Fig. 9). In Jura Ost there are four cycles in the upper part and in Nördlich Lägern and Zürich Nordost five. Bläsi (1987) already mentioned four cycles for RIN and five for WEI, which fits with the observations in this study. This description fits with the observations for marker Bed-VI which is not existing in Jura Ost (BOZ2, BOZ1 and RIN, condensation at the top OPA). Overall, each small-scaled coarsening-upward trend can be interpreted as a regressive trend, linked to a relative sea level fall or sediment supply outpacing the amount of accommodation generated during a relative sea level rise.

It can be questioned if the coarsening-upward cycles within the OPA represents 4th or 5th order cycles. In the homogeneous clay mineral-rich part of the Opalinuston Formation in southern Germany, Leu et al. (2023) detected many more cycles (frequencies: 0.01–0.45 1/m) using gamma-ray downhole logging data reflecting chemical/physical heterogeneities related to variations in grain size, clay content and organic content. Leu et al. (2023) evidenced the orbital forcing of the sedimentation patterns reflected in the gamma-ray signals with a periodicity of resp. 20 ka, 100 ka or 400 ka (see also Wetzel & Allia, 2003). This might be the case for the smaller-scaled coarsening-upward cycles but further studies are necessary to confirm this. Already Bläsi (1987) mentioned that coarsening-upward trends interpreted as shallowing-upward regressive cycles in the OPA can be triggered by eustatic sea level fluctuations linked to changes in insolation.

5.3.2 General coarsening-upward sequences

Small-scale coarsening-upward cycles stack together in two long-term overall coarsening-upward sequences within the OPA (Fig. 9). One sequence is present from the base of the OPA to the top of the FA silty, and the second sequence from the base to the top of the FA calcareous beds. Lauper et al. (2018, 2021b) observed in the OPA, described from core sections in western Switzerland (Mont Terri rock laboratory), also two coarsening-upward sequences.

At the largest scale, the full OPA can be interpreted as one overall long-term coarsening-upward sequence with the presence of iron-oolites at the top (transition to the Passwang Formation and its eastern equivalents).

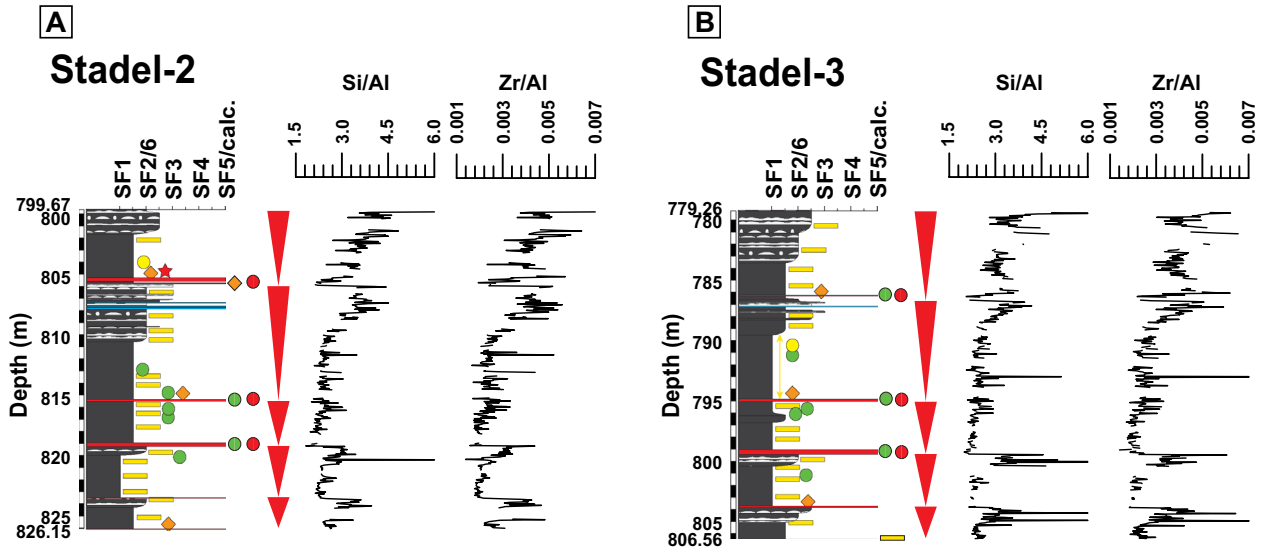

Fig. 10 Coarsening-upward cycles (red triangle) in the upper part of the OPA drill cores in the FA calcareous beds of STA2 (**A**) and STA3 (**B**). The small-scale cycles are often characterised by calcareous beds at the top and high Si/Al and Zr/Al ratios

Burkhalter (1995, 1996) and Lauper et al. (2021a) interpreted the transition of the OPA and its upper bounding unit as a period of sediment non-deposition being the result of sediment bypassing during a significant regressive- and shallowing-upward trend (also seen by Bläsi, 1987; Lauper et al., 2021b). Zimmermann et al. (2015, 2018) also detected a pronounced shallowing-upward trend in the German Basin for the entire Opalinum Zone. Additionally, Zimmermann et al. (2015) showed that the North Sea, Denmark and the Polish Basin (further south-east it is different) represent similar pronounced regressive phases during the Lower Aalenian (Opalinum Zone). Overall, the large-scale coarsening-upward trends are interpreted as being formed during regressive phases topped by low relative sea levels, often resulting in non-deposition or erosion. However, it should be mentioned that due to insufficient temporal constraints, the authors refrain from using a classical sequence stratigraphic approach (e.g., Mitchum & Van Wagoner, 1991; Miall, 2010; Magalhães et al., 2020; Fragoso et al., 2021; Catuneanu, 2019a, 2019b, 2022).

5.3.3 From regional signal to global trend

Overall, the observed smaller-scaled coarsening-upward cycles and larger-scale coarsening-upward sequences represent shallowing-upward regressive trends. Factors steering those shallowing-upward trends result from the interplay between different parameters, such as variations in accommodation space affected by sediment supply, subsidence or uplift (linked to basin tectonics), and eustatic sea level change. However, also other factors may control the observed facies variations such as compaction, the slope gradient of the epicontinental basin during the Aalenian, regional and global climate change (humidity, insolation, vegetation, weathering, reworking, erosion), and physical processes within the OPA basin influencing sediment distribution (storm, wave, wind, currents, mass flows), water chemistry and internal dynamics (Bayer & McGhee, 1985; Reading, 1996; Allen & Allen, 2005; Colombera & Mountney, 2020).

Although it is difficult to detangle the effect of different controlling parameters on the observed facies variations, some aspects could be discussed such as palaeogeography, synsedimentary subsidence, and climate change, both from a regional and global perspective.

Large-scale coarsening-upward trends, as well as lateral facies variations could be explained by changing palaeogeographical settings. For example, the central North Sea dome's uplift influenced the deposition in the OPA basin during the Early Aalenian. The formation of the thermally driven doming began in the Late Toarcian and had its greatest extent in the Early Aalenian, leading to the separation of the seaway between the Tethys and the Boreal Sea (Underhill & Partington, 1993). The doming is linked with critical erosive events (Underhill & Partington, 1993; Callomon, 2003), an important sediment source. Moreover, when the Tethys Ocean and the Boreal Arctic Sea were connected via the Laurasian Seaway (Bjerrum et al., 2001; Callomon, 2003; Zimmermann et al., 2015), southward-directed longshore currents with cold water from the Arctic Sea could have influenced the deposition of the OPA (Bjerrum et al., 2001). Those currents are linked to hydrostatic relative sea level differences between the Tethys and the Arctic Sea (Bjerrum et al.,

2001). The palaeogeographic distribution and gateways to the open ocean define current circulation patterns and the provenance of the sediments, which could explain vertical and lateral west–east differentiation between the studied cores. The provenance of the OPA sediments is highly debated. Wetzel & Allia (2000, 2003) and Wetzel et al. (2003) mention the Scandinavian, the Bohemian Massif, the London-Brabant Massif, the Rhenish Massif, and subordinately the Alemannic Islands as possible sediment sources. However, those land masses are localised tens to hundreds of km from the depositional area, and as such their relative contribution as sediment source is questioned.

Another factor which is often debated is the role of synsedimentary subsidence in the Aalenian. Many studies evidence that the Swiss Swabian Basin was undoubtedly exposed to synsedimentary subsidence in the Aalenian (e.g., Wetzel & Allia, 2003). The subsidence rate at the beginning of the Aalenian (Opalinum Subzone, lower part of the OPA) had to be greater than or equal to the sedimentation rate due to the enormous increase in sedimentation thickness from the Gross Wolf Member to the OPA. Also, this study shows small thickness variations certainly within the lower part of the OPA which could be also explained by synsedimentary subsidence.

Within the upper part of the cores, an increase in illite/kaolinite values is often measured and detected (Mäder et al., 2021; Aschwanden et al., 2021, 2022; Gimmi et al., 2022; Wersin et al., 2022; Zwahlen et al., 2022; Gaucher et al., 2023; Mazurek et al., 2021, 2023). This increase in illite/kaolinite can be linked to increased chemical weathering due to humid climate conditions and/or a change in sediment provenance. Therefore, they are often used as a proxy for understanding chemical weathering intensity (linked to climate change) and sediment provenance. Ruffell et al. (2002), Dera et al. (2009), Fredin et al. (2017), Corentin et al. (2020), and Blok et al. (2023 and references therein) evidence this in similar clay formations. Climate change might be more important in the OPA than previously thought, affecting mineralogy and impacting the small-scaled coarsening-upward cycles and larger-scale coarsening-upward sequences.

Global warming and increased chemical weathering and anoxic conditions occurred in the Early Toarcian (Fantasia et al., 2018; Fernandez et al., 2021). After the Toarcian Oceanic Anoxic Event (T-OAE CIE, also called Jenkyns event), a general cooling in the Aalenian followed (Nikitenko et al., 2008; Pieńkowski et al., 2008). Global cooling, polar glaciation, and a drop in sea water temperatures were proposed for the Aalenian (Rogov & Zakharov, 2010; Korte et al., 2015; Zimmermann et al., 2015, 2018). At the beginning of the Aalenian, a mid-latitude cooling of 10 °C in the Laurasian Seaway was reconstructed using oxygen isotopes (Korte et al., 2015). Similar results were determined in the southern Laurasian Seaway (northern Spain), where an average sea water temperature of 15.7 °C was measured in the Bifidatum Subzone (Gómez et al., 2009). This cooling lasted throughout the Aalenian, with a short warming event within the Bradfordensis Zone (Fig. 1C), until the end of the Aalenian and the beginning of the Bajocian, when new warming started (Gómez et al., 2009). Gómez et al. (2009) postulated that those cooling and warming events in several European localities could be of global extent. The Aalenian cooling was probably caused by the southward inflow of boreal waters through the Laurasian Seaway. In contrast, the large temperature spread might have been caused by the short-term inflow of warm Tethyan waters. Consequently, temperate (if not boreal) climatic conditions are likely to have occurred in the study area. This would mean that the whole OPA would have been deposited during rather cold climate conditions but had again a warming boost at the end of the Opalinum Zone, corresponding to the increase in illite/kaolinite and potentially changing current patterns. This could explain the large-scaled coarsening-upward trend. However, more studies are necessary to detangle global climate change from regional and local factors (including synsedimentary subsidence, palaeogeographic configuration in an epicontinental sea, current strength and patterns, and sediment input) in the OPA.

6 Conclusion

Six distinct subfacies and six additional lithologies within the OPA and its bounding units, including the uppermost two members of the Staffelegg Formation underneath, as well as the lowermost members of the overlying Passwang Formation and its eastern equivalents, were applied to characterise the OPA in Switzerland. This scheme also has the potential to be applied to other mudstone formations. Detailed descriptions of subfacies and additional lithologies are crucial for assessing and understanding regional-scale variations in facies, both vertically and laterally. The mineralogical data obtained through XRD and MM, and the geochemical data from XRF are appropriate for quantifying the lithological variability within the OPA. They can be associated with the different subfacies/lithologies and facies associations. Non-metric multidimensional scaling analyses have statistically demonstrated that subfacies/lithologies can be distinguished using Si/Al, Zr/Al, Ca/Al, and Fe/Al. Furthermore, an additional subfacies (SF6) within the OPA refers to mass-wasting deposits.

The high-quality cores drilled closely together are unique for detailed vertical and lateral facies variability studies. Several small-scale, 1–64 m thick,

coarsening-upward cycles are defined within the OPA, represented mainly by successions going from SF1 towards SF2, an increase in Si/Al and Zr/Al and often topped by calcareous beds. The coarsening-upward cycles (six to seven cycles) are interpreted as regressive trends, the top of this trend representing the lowest relative sea level and a break in sedimentation. Smaller coarsening-upward cycles stack together in two overall coarsening-upward sequences throughout the full OPA. Six correlation beds are identified in the OPA of which one is of stratigraphic and global significance combining lithology with biostratigraphy and chemostratigraphy. Overall, it should be mentioned that the observed regressive trends and facies variations are influenced by many factors such as, e.g., synsedimentary subsidence or tectonics, eustatic sea level change, provenance and delivery of sediments, the palaeogeographical setting, possible gateways to the open ocean influencing the bottom current circulation, and climate change. Finally, the current dynamics in the OPA has been clearly underestimated until now and the existing depositional models for the Aalenian should be questioned.

Supplementary Information

The online version contains supplementary material available at https://doi.org/10.1186/s00015-024-00463-6.

Additional file 1: Overview of the Opalinus Clay succession in the thirteen drill cores. The RHE1 core has been drilled obliquely but represented here as true vertical depth. Main formations, members, and the four facies associations within the OPA are indicated. Ten subfacies/lithologies are differentiated in the cores (see legend). Additional attributes such as the presence of siderite nodules, siderite layers, calcareous concretions, bioclastic debris, tilted beds, phosphate traces, fossils, and calcitic recrystalised iron-ooids are visualised by individual symbols at a depth of occurrence (see legend). Reference cores are indicated with stars (cfr. descriptions based on high-quality slabs). The uppermost limestone bed in SLA1 (835.05 m) has been described as top OPA, not 831.40 m as mentioned in the original report (Albert et al., 2012). This new described top fits with the C-isotope shift ($\delta^{13}C_{org}$) at the top of the OPA as observed in MAR1, BEN and TRU1 (Wohlwend et al., 2024). The lithology for the «Murchisonae-Oolith Formation» described in SLA1 fits well with the lithology described in MAR1 to TRU1, except that this formation is a little thicker in SLA1. Moreover, the top OPA in RIN and WEI has also been adapted from the original reports (Matter et al., 1987, 1988; adapted version already in Wohlwend et al., 2024).

Acknowledgements
We thank Wilfried Winkler and Daniel Marty for editorial handling and two anonymous reviewers for the constructive reviews. The authors thank the University of Bern (Rock-water interaction group) for the XRD measurements; Geotek Ltd. (UK) is highly acknowledged for providing the X-ray fluorescence measurements; Nagra and Ad Terra Energy for the multi-mineral interpretation analysis; NiMBUC Geoscience (AUT) for the bedding measurements and Raphael Schneeberger for the discussions on the data and the Nagra team for their technical and logistical support and always the open ear for discussion. Michele Claps is thanked for the comments on an earlier version of the manuscript. Bruno Lauper and David Jaeggi are thanked for the fruitful discussions about the OPA lithologies and subfacies classification. Financial support is gratefully provided by Nagra and the University of Fribourg.

Author contributions
GNZ: data analysis, interpretation, writing, discussion, editing figures; SW, GD, AF: data analysis, interpretation, writing, discussion; FF, JB: data analysis; AW: data analysis, interpretation, writing, discussion. All authors read the article, discussed the results, and provided critical feedback. All authors read and approved the final manuscript.

Funding
This work has been funded by Nagra and the University of Fribourg.

Availability of data and materials
The datasets used and/or analysed during this study are either included in this manuscript and its supplementary material or can be requested from the authors.

Declarations

Consent for publication
All authors have given their consent for publication.

Competing interests
The authors declare that they have no competing interests.

Author details
[1]Department of Geosciences, University of Fribourg, Chemin du Musée 6, 1700 Fribourg, Switzerland. [2]Institute of Geological Sciences, University of Bern, Baltzerstrasse 1 + 3, 3012 Bern, Switzerland. [3]National Cooperative for the Disposal of Radioactive Waste (Nagra), Hardstrasse 73, 5430 Wettingen, Switzerland. [4]Department of Environmental Sciences, University of Basel, Bernoullistrasse 32, 4056 Basel, Switzerland.

Received: 23 February 2024 Accepted: 23 May 2024
Published online: 12 September 2024

References

Albert, W., Bläsi, H.R., Madritsch, H., Vogt, T., & Weber, H.P. (2012). Geologie, Stratigraphie, Strukturgeologie, bohrlochgeophysikalisches Logging und Wasserproben der Geothermiebohrung Schlattingen SLA-1 (Rohdaten). *Nagra Project Report, NPB 12–16,* Nagra, Wettingen, Switzerland. Available at nagra.ch.

Allen, P. A., & Allen, J. R. (2005). *Basin analysis: principles and applications* (2nd ed.). Blackwell Science.

Allia, V. (1996). Sedimentologie und Ablagerungsgeschichte des Opalinustons in der Nordschweiz. *PhD Thesis.* University of Basel, Basel, Switzerland.

Alsop, G. I., & Weinberger, R. (2020). Are slump folds reliable indicators of downslope flow in recent mass transport deposits? *Journal of Structural Geology, 135,* 104037. https://doi.org/10.1016/j.jsg.2020.104037

Aschwanden, L., Camesi, L., Gimmi, T., Jenni, A., Kiczka, M., Mäder, U., Mazurek, M., Rufer, D., Waber, H.N., Wersin, P., Zwahlen, C., & Traber, D. (2021). TBO Trüllikon-1-1: Data Report, Dossier VIII: Rock properties, porewater characterisation and natural tracer profiles. *Nagra Arbeitsbericht, NAB 20-09,* Nagra, Wettingen, Switzerland. Available at nagra.ch.

Aschwanden, L., Camesi, L., Gaucher, E., Gimmi, T., Jenni, A., Kiczka, M., Mäder, U., Mazurek, M., Rufer, D., Waber, H.N., Wersin, P., Zwahlen, C., & Traber, D. (2022). TBO Stadel-3-1: Data Report, Dossier VIII: Rock properties, porewater characterisation and natural tracer profiles. *Nagra Arbeitsbericht, NAB 22-01,* Nagra, Wettingen, Switzerland. Available at nagra.ch.

Bayer, U., & McGhee, G. R. (1985). Evolution in marginal epicontinental basins: the role of phylogenetic and ecological factors: Ammonite replacements in the German Lower and Middle Jurassic. In U. Bayer & A. Seilacher (Eds.), *Sedimentary and Evolutionary Cycles. Lecture Notes in Earth Sciences, 1* (pp. 163–220). Berlin: Springer. https://doi.org/10.1007/BFb0009843

Bellwald, B., Nigg, V., Fabbri, S. C., Becker, L. W. M., Gilli, A., & Anselmetti, F. S. (2024). Holocene seismic activity in south-eastern Switzerland: Evidence from the sedimentary record of Lake Silvaplana. *Sedimentology, 71,* 116–151. https://doi.org/10.1111/sed.13131

Bjerrum, C. J., Surlyk, F., Callomon, J. H., & Slingerland, R. L. (2001). Numerical paleoceanographic study of the Early Jurassic transcontinental Laurasian Seaway. *Paleoceanography, 16*(4), 390–404. https://doi.org/10.1029/2000PA000512

Bläsi, H.R., Deplazes, G., Schnellmann, M., & Traber, D. (2013). Sedimentologie und Stratigraphie des 'Braunen Doggers' und seiner westlichen Äquivalente. *Nagra Arbeitsbericht, NAB 12-51,* Nagra, Wettingen, Switzerland. Available at nagra.ch.

Bläsi, H. R. (1987). Lithostratigraphie und Korrelation der Doggersedimente in den Bohrungen Weiach, Riniken Und Schafisheim. *Eclogae Geologicae Helvetiae, 80*(2), 415–430.

Blok, C. N., Adatte, T., Ineson, J. R., Sheldon, E., Jelby, M. E., Smit, F. W. H., Lauridsen, B. W., Anderskouv, K., & Bodin, S. (2023). Clay mineral assemblages as a tool in source-to-sink studies: an example from the Lower Cretaceous of the North Sea Basin. *Bulletin of the Geological Society of Denmark, 71*, 99–113. https://pub.geus.dk/en/publications/clay-mineral-assemblages-as-a-tool-in-source-to-sink-studies-an-e

Bohacs, K. M., Lazar, O. R., & Demko, T. M. (2014). Parasequence types in shelfal mudstone strata—quantitative observations of lithofacies and stacking patterns, and conceptual link to modern depositional regimes. *Geology, 42*(2), 131–134. https://doi.org/10.1130/G35089.1

Bossart, P., & Thury, M. (2008). Mont Terri rock laboratory. Project, programme 1996 to 2007 and results. *Reports of the Swiss Geological Survey, No. 3,* Federal Office of Topography Swisstopo, Wabern, Switzerland.

Bossart, P., Bernier, F., Birkholzer, J., Bruggeman, C., Connolly, P., Dewonck, S., Fukaya, M., Herfort, M., Jensen, M., Matray, J.-M., Mayor, J. C., Moeri, A., Oyama, T., Schuster, K., Shigeta, N., Vietor, T., & Wieczorek, K. (2017). Mont Terri rock laboratory, 20 years of research: Introduction, site characteristics and overview of experiments. *Swiss Journal of Geosciences, 110*, 3–22. https://doi.org/10.1007/s00015-016-0236-1

Burkhalter, R. M. (1995). Ooidal ironstones and ferruginous microbialites: Origin and relation to sequence stratigraphy (Aalenian and Bajocian, Swiss Jura mountains). *Sedimentology, 42*, 57–74. https://doi.org/10.1111/j.1365-3091.1995.tb01271.x

Burkhalter, R. M. (1996). Die Passwang-Alloformation (unteres Aalénien bis unteres Bajocien) im zentralen und nördlichen Schweizer Jura. *Eclogae Geologicae Helveticae, 89*(3), 875–934. https://doi.org/10.5169/seals-167927

Buso, V. V., Milana, J. P., Sobiesiak, M. S., & Kneller, B. (2019). The carboniferous MTD complex at La Peña Canyon, Paganzo Basin (San Juan, Argentina). In K. Ogata, A. Festa, & G. A. Pini (Eds.), *Submarine landslides: Subaqueous mass transport deposits from outcrops to seismic profiles* (pp. 105–116). USA: Wiley. https://doi.org/10.1002/9781119500513.ch7

Callomon, J. H. (2003). The Middle Jurassic of western and northern Europe: Its subdivisions, geochronology and correlations. *Geological Survey of Denmark and Greenland Bulletin, 1*, 61–73. https://doi.org/10.34194/geusb.v1.4648

Calvert, S. E., & Pedersen, T. F. (2007). Chapter fourteen: Elemental proxies for palaeoclimatic and palaeoceanographic variability in marine sediments: Interpretation and application. *Developments in Marine Geology, 1*, 567–644. https://doi.org/10.1016/S1572-5480(07)01019-6

Catuneanu, O. (2019a). Model-independent sequence stratigraphy. *Earth-Science Reviews, 188*, 312–388. https://www.sciencedirect.com/science/article/pii/S0012825218305993

Catuneanu, O. (2019b). Scale in sequence stratigraphy. *Marine and Petroleum Geology, 106*, 128–159. https://www.sciencedirect.com/science/article/pii/S026481721930176X

Catuneanu, O. (2022). *Principles of Sequence Stratigraphy* (2nd ed.). Elsevier

Clarke, S., Hubble, T., Airey, D., Yu, P., Boyd, R., Keene, J., Exon, N., Gardner, J., Party, S., Shipboard Party SS12/2008, et al. (2012). Chapter 5: Submarine landslides on the upper southeast Australian passive continental margin—preliminary findings. In Y. Yamada (Ed.), *Submarine mass movements and their consequences: advances in natural and technological hazards research, 31, 5th International Symposium* (pp. 55–66). Dordrecht: Springer. https://doi.org/10.1007/978-94-007-2162-3_5

Colombera, L., & Mountney, N. P. (2020). Accommodation and sediment-supply controls on clastic parasequences: A meta-analysis. *Sedimentology, 67*, 1667–1709. https://doi.org/10.1111/sed.12728

Corentin, P., Deconinck, J.-F., Pellenard, P., Amédro, F., Bruneau, L., Chenot, E., Matrion, B., Huret, E., & Landrein, P. (2020). Environmental and climatic controls of the clay mineralogy of Albian deposits in the Paris and Vocontian basins (France). *Cretaceous Research, 108*, 104342. https://doi.org/10.1016/j.cretres.2019.104342

Craigie, N. W., & Rees, A. J. (2016). Chemostratigraphy of glaciomarine sediments in the Sarah Formation, northwest Saudi Arabia. *Journal of African Earth Sciences, 117*, 263–284. https://doi.org/10.1016/j.jafrearsci.2016.02.006

Cresta, S., Goy, A., Ureta, S., Arias, C., Barrón, E., Bernad, J., Canales, M. L., García-Joral, F., García-Romero, E., Gialanella, P. R., Gómez, J. J., González, J. A., Herrero, C., Martínez, G., Osete, M. L., Perilli, N., & Villalaín, J. J. (2001). The global boundary stratotype section and point (GSSP) of the Toarcian-Aalenian boundary (Lower-Middle Jurassic). *Episodes Journal of International Geoscience, 24*(3), 166–175. https://doi.org/10.18814/epiiugs/2001/v24i3/003

Croudace, I. W., Löwemark, L., Tjallingii, R., & Zolitschka, B. (2019). Current perspectives on the capabilities of high resolution XRF core scanners. *Quaternary International, 514*, 5–15. https://doi.org/10.1016/j.quaint.2019.04.002

Dera, G., Brigaud, B., Monna, F., Laffont, R., Pucéat, E., Deconinck, J.-F., Pellenard, P., Joachimski, M. M., & Durlet, C. (2011). Climatic ups and downs in a disturbed Jurassic world. *Geology, 39*(3), 215–218. https://doi.org/10.1130/G31579.1

Dera, G., Pellenard, P., Neige, P., Deconinck, J.-F., Pucéat, E., & Dommergues, J.-L. (2009). Distribution of clay minerals in Early Jurassic Peritethyan seas: Palaeoclimatic significance inferred from multiproxy comparisons. *Palaeogeography, Palaeoclimatology, Palaeoecology, 271*, 39–51. https://doi.org/10.1016/j.palaeo.2008.09.010

Dietze, V., Gräbenstein, S., Franz, M., Schweigert, G., & Wetzel, A. (2021). The Middle Jurassic Opalinuston Formation (Aalenian, Opalinum Zone) at its type locality near Bad Boll and adjacent outcrops (Swabian Alb, SW Germany). *Palaeodiversity, 14*, 15–113. https://doi.org/10.18476/pale.v14.a3

Ebert, A., Gregorczyk, L., Hägerstedt, E., & Gysi, M. (2021b). TBO Bülach-1-1: Data Report, Dossier V: Structural geology. *Nagra Arbeitsbericht, NAB 20-08,* Nagra, Wettingen, Switzerland. Available at nagra.ch.

Ebert, A., Gregorczyk, L., Hägerstedt, E., Cioldi, S., & Gysi, M. (2021c). TBO Marthalen-1-1: Data Report, Dossier V: Structural geology. *Nagra Arbeitsbericht, NAB 21-20,* Nagra, Wettingen, Switzerland. Available at nagra.ch.

Ebert, A., Cioldi, S., Gregorczyk, L., Rust, S., Böhni, D., & Gysi, M. (2021a). TBO Trüllikon-1-1: Data Report, Dossier V: Structural geology. *Nagra Arbeitsbericht, NAB 20-09,* Nagra, Wettingen, Switzerland. Available at nagra.ch.

Ebert, A., Gregorczyk, L., Cioldi, S., Hägerstedt, E., & Gysi, M. (2022d). TBO Bözberg-2-1: Data Report, Dossier V: Structural geology. *Nagra Arbeitsbericht, NAB 21-22,* Nagra, Wettingen, Switzerland. Available at nagra.ch.

Ebert, A., Gregorczyk, L., Cioldi, S., Hägerstedt, E., & Gysi, M. (2022c). TBO Bözberg-1-1: Data Report, Dossier V: Structural geology. *Nagra Arbeitsbericht, NAB 21-21,* Nagra, Wettingen, Switzerland. Available at nagra.ch.

Ebert, A., Cioldi, S., Hägerstedt, E., & Gysi, M. (2022a). TBO Stadel-3-1: Data Report, Dossier V: Structural geology. *Nagra Arbeitsbericht, NAB 22-01,* Nagra, Wettingen, Switzerland. Available at nagra.ch.

Ebert, A., Cioldi, S., Hägerstedt, E., & Weber, H.P. (2022b). TBO Stadel-2-1: Data Report, Dossier V: Structural geology. *Nagra Arbeitsbericht, NAB 22-02,* Nagra, Wettingen, Switzerland. Available at nagra.ch.

Ebert, A., Hägerstedt, E., Cioldi, S., Gregorczyk, L., & Casanova, F. (2023b). TBO Bachs-1-1: Data Report, Dossier V: Structural geology. *Nagra Arbeitsbericht, NAB 22-04,* Nagra, Wettingen, Switzerland. Available at nagra.ch.

Ebert, A., Cioldi, S., Hägerstedt, E., Gregorczyk, L., & Casanova, F. (2023a). TBO Rheinau-1-1: Data Report, Dossier V: Structural geology. *Nagra Arbeitsbericht, NAB 22-03,* Nagra, Wettingen, Switzerland. Available at nagra.ch.

Etter, W. (1990). Paläontologische Untersuchungen im unteren Opalinuston der Nordschweiz. *PhD Thesis.* University of Zurich, Zürich, Switzerland.

Fantasia, A., Föllmi, K. B., Adatte, T., Spangenberg, J. E., & Montero-Serrano, J.-C. (2018). The Early Toarcian oceanic anoxic event: Paleoenvironmental and paleoclimatic change across the Alpine Tethys (Switzerland). *Global and Planetary Change, 162*, 53–68. https://doi.org/10.1016/j.gloplacha.2018.01.008

Fantasia, A., Mattioli, E., Spangenberg, J. E., Adatte, T., Bernárdez, E., Ferreira, J., Thibault, N., Krencker, F.-N., & Bodin, S. (2022). The Middle-Late Aalenian event: A precursor of the Mesozoic Marine Revolution. *Global and Planetary Change, 208*, 103705. https://doi.org/10.1016/j.gloplacha.2021.103705

Feist-Burkhardt, S. (2012). Palynostratigraphie des Mittleren Jura: Teil I—Bohrungen Benken, Schlattingen-1 und Weiach sowie einige Aufschlussproben der Lägern und deren Korrelation, Teil II—Bohrung Riniken, Aufschlussproben Bernhardholz, Dangstetten und Lägern. *Nagra Arbeitsbericht, NAB 12-57,* Nagra, Wettingen, Switzerland. Available at nagra.ch.

Fernandez, A., Korte, C., Ullmann, C. V., Looser, N., Wohlwend, S., & Bernasconi, S. M. (2021). Reconstructing the magnitude of Early Toarcian (Jurassic) warming using the reordered clumped isotope compositions of belemnites. *Geochimica Et Cosmochimica Acta, 293*, 308–327. https://doi.org/10.1016/j.gca.2020.10.005

Field, M. E., Gardner, J. V., Jennings, A. E., & Edwards, B. D. (1982). Earthquake-induced sediment failures on a 0.25° slope, Klamath river delta, California. *Geology, 10*, 542–546. https://doi.org/10.1130/0091-7613(1982)10%3c542:ESFOAS%3e2.0.CO;2

Föllmi, K. B. (2016). Sedimentary condensation. *Earth-Science Reviews, 152*, 143–180. https://doi.org/10.1016/j.earscirev.2015.11.016

Fragoso, D. G. C., Raja Gabaglia, G. P., Magalhães, A. J. C., & Dos Santos Scherer, C. M. (2021). Cyclicity and hierarchy in sequence stratigraphy: an integrated approach. *Brazilian Journal of Geology, 51*(2), e20200106. https://www.scielo.br/j/bjgeo/a/Ht9mRFQW8dJssbGm3VJjx7H/

Franz, M., & Nitsch, E. (2009). Zur lithostratigraphischen Gliederung des Aalenium in Baden-Württemberg. *Landesamt Für Geologie, Rohstoffe Und Bergbau - Informationen, 22*, 123–146.

Fredin, O., Viola, G., Zwingmann, H., Sørlie, R., Brönner, M., Lie, J.-E., Grandal, E. M., Müller, A., Margreth, A., Vogt, C., & Knies, J. (2017). The inheritance of a Mesozoic landscape in western Scandinavia. *Nature Communications, 8*, 14879. https://doi.org/10.1038/ncomms14879

Füchtbauer, H. (1988). *Sedimente und Sedimentgesteine—Sediment-Petrologie, Teil II* (4th ed.). Schweizerbartsche Verlagsbuchhandlung.

García-Tortosa, F. J., Alfaro, P., Gibert, L., & Scott, G. (2011). Seismically induced slump on an extremely gentle slope (<1°) of the Pleistocene Tecopa paleolake (California). *Geology, 39*(11), 1055–1058. https://doi.org/10.1130/G32218.1

Gaucher, E., Aschwanden, L., Gimmi, T., Jenni, A., Kiczka, M., Mazurek, M., Wersin, P., Zwahlen, C., Mäder, U., & Traber, D. (2023). TBO Bachs-1-1: Data Report, Dossier VIII: Rock properties, porewater characterisation and natural tracer profiles. *Nagra Arbeitsbericht, NAB 22-04,* Nagra, Wettingen, Switzerland. Available at nagra.ch.

Gibert, L., Alfaro, P., García-Tortosa, F. J., & Scott, G. (2011). Superposed deformed beds produced by single earthquakes (Tecopa basin, California): Insights into paleoseismology. *Sedimentary Geology, 235*, 148–159. https://doi.org/10.1016/j.sedgeo.2010.08.003

Gimmi, T., Aschwanden, L., Gamesi, L., Gaucher, E., Jenni, A., Kiczka, M., Mäder, U., Mazurek, M., Rufer, D., Waber, H.N., Wersin, P., Zwahlen, C., & Traber, D. (2022). TBO Bözberg-2-1: Data Report, Dossier VIII: Rock properties, porewater characterisation and natural tracer profiles. *Nagra Arbeitsbericht, NAB 21-22,* Nagra, Wettingen, Switzerland. Available at nagra.ch.

Gómez, J. J., Canales, M. L., Ureta, S., & Goy, A. (2009). Palaeoclimatic and biotic changes during the Aalenian (Middle Jurassic) at the southern Laurasian Seaway (Basque–Cantabrian basin, northern Spain). *Palaeogeography, Palaeoclimatology, Palaeoecology, 275*, 14–27. https://doi.org/10.1016/j.palaeo.2009.01.009

Haq, B. U. (2018). Jurassic sea-level variations: A reappraisal. *The Geological Society of America, GSA Today, 28*(1), 4–10. https://doi.org/10.1130/GSATG359A.1

Haq, B. U., Hardenbol, J., & Vail, P. R. (1987). Chronology of fluctuating sea levels since the Triassic. *Science, 235*, 1156–1167. https://doi.org/10.1126/science.235.4793.1156

Hardenbol, J., Thierry, J., Farley, M. B., Jacquin, T., De Graciansky, P.-C., & Vail, P. R. (1998). Mesozoic and Cenzoic sequence chronostratigraphic framework of European basins. *Society for Sedimentary Geology (SEPM) Special Publication, 60*, 3–13. https://archives.datapages.com/data/sepm_sp/SP60/Mesozoic_and_Cenozoic_Sequence_Chronostratigraphic.htm

Hieke, W. (1984). A thick Holocene homogenite from the Ionian Abyssal Plain (eastern Mediterranean). *Marine Geology, 55*, 63–78. https://doi.org/10.1016/0025-3227(84)90133-6

Hieke, W., & Werner, F. (2000). The Augias megaturbidite in the central Ionian Sea (central Mediterranean) and its relation to the Holocene Santorini event. *Sedimentary Geology, 135*, 205–218. https://doi.org/10.1016/S0037-0738(00)00072-5

Hostettler, B., Dietze, V., Jaeggi, D., & Menkveld-Gfeller, U. (2020). SO-C Experiment: Ammonite stratigraphy and fossils of the Passwang Formation (Middle Jurassic) and the Opalinus Clay (Lower to Middle Jurassic) excavated in Ga 18 and the Niches P3, Passwang and CO_2 in the Mont Terri rock laboratory. *Mont Terri Technical Report, TR 2018-01*. Federal Office of Topography Swisstopo, Wabern, Switzerland.

Hostettler, B., Reisdorf, A. G., Jaeggi, D., Deplazes, G., Bläsi, H. R., Morard, A., Feist-Burkhardt, S., Waltschew, A., Dietze, V., & Menkveld-Gfeller, U. (2017). Litho- and biostratigraphy of the Opalinus Clay and bounding formations in the Mont Terri rock laboratory (Switzerland). *Swiss Journal of Geosciences, 110*, 23–37. https://doi.org/10.1007/s00015-016-0250-3

Huang, C. (2018). Chapter two—Astronomical time scale for the Mesozoic. *Stratigraphy & Timescales, 3*, 81–150. https://doi.org/10.1016/bs.sats.2018.08.005

Huhn, K., Arroyo, M., Cattaneo, A., Clare, M. A., Gràcia, E., Harbitz, C. B., Krastel, S., Kopf, A., Løvholt, F., Rovere, M., Strasser, M., Talling, P. J., & Urgeles, R. (2019). Modern submarine landslide complexes: A short review. In K. Ogata, A. Festa, & G. A. Pini (Eds.), *Submarine landslides: Subaqueous mass transport deposits from outcrops to seismic profiles* (pp. 183–200). Wiley. https://doi.org/10.1002/9781119500513.ch12

Jaeggi, D., Bossart, P., & Wymann, L. (2014). Kompilation der lithologischen Variabilität und Eigenschaften des Opalinus-Ton im Felslabor Mont Terri. *Expert Report for ENSI, 09-08,* Federal Office of Topography Swisstopo, Wabern, Switzerland.

Jordan, P., Schürch, P., Naef, H., Schwarz, M., Felber, R., Ibele, T., & Gysi, M. (2021b). TBO Marthalen-1-1: Data Report, Dossier III: Lithostratigraphy. *Nagra Arbeitsbericht, NAB 21-20,* Nagra, Wettingen, Switzerland. Available at nagra.ch.

Jordan, P., Naef, H., Schürch, P., Schwarz, M., Ibele, T., Felber, R., & Gysi, M. (2021a). TBO Bülach-1-1: Data Report, Dossier III: Lithostratigraphy. *Nagra Arbeitsbericht, NAB 20-08,* Nagra, Wettingen, Switzerland. Available at nagra.ch.

Jordan, P., Schürch, P., Naef, H., Schwarz, M., Felber, R., Ibele, T., & Weber, H.P. (2022b). TBO Stadel-2-1: Data Report, Dossier III: Lithostratigraphy. *Nagra Arbeitsbericht, NAB 22-02,* Nagra, Wettingen, Switzerland. Available at nagra.ch.

Jordan, P., Schürch, P., Naef, H., Schwarz, M., Felber, R., Ibele, T., & Gysi, M. (2022a). TBO Bözberg-2-1: Data Report, Dossier III: Lithostratigraphy. *Nagra Arbeitsbericht, NAB 21-22,* Nagra, Wettingen, Switzerland. Available at nagra.ch.

Jordan, P., Schürch, P., Schwarz, M., Felber, R., Naef, H., Ibele, T., & Casanova, F. (2023). TBO Bachs-1-1: Data Report, Dossier III: Lithostratigraphy. *Nagra Arbeitsbericht, NAB 22-04,* Nagra, Wettingen, Switzerland. Available at nagra.ch.

Kaehr, D., & Gysi, M. (2021c). TBO Trüllikon-1-1: Data Report, Dossier II: Core photography. *Nagra Arbeitsbericht, NAB 20-09,* Nagra, Wettingen, Switzerland. Available at nagra.ch.

Kaehr, D., & Gysi, M. (2021b). TBO Marthalen-1-1: Data Report, Dossier II: Core photography. *Nagra Arbeitsbericht, NAB 21-20,* Nagra, Wettingen, Switzerland. Available at nagra.ch.

Kaehr, D., & Gysi, M. (2021a). TBO Bülach-1-1: Data Report, Dossier II: Core photography. *Nagra Arbeitsbericht, NAB 20-08,* Nagra, Wettingen, Switzerland. Available at nagra.ch.

Kaehr, D., & Gysi, M. (2022c). TBO Stadel-2-1: Data Report, Dossier II: Core photography. *Nagra Arbeitsbericht, NAB 22-02,* Nagra, Wettingen, Switzerland. Available at nagra.ch.

Kaehr, D., & Gysi, M. (2022d). TBO Stadel-3-1: Data Report, Dossier II: Core photography. *Nagra Arbeitsbericht, NAB 22-01,* Nagra, Wettingen, Switzerland. Available at nagra.ch.

Kaehr, D., & Gysi, M. (2022a). TBO Bözberg-1-1: Data Report, Dossier II: Core photography. *Nagra Arbeitsbericht, NAB 21-21,* Nagra, Wettingen, Switzerland. Available at nagra.ch.

Kaehr, D., & Gysi, M. (2022b). TBO Bözberg-2-1: Data Report, Dossier II: Core photography. *Nagra Arbeitsbericht, NAB 21-22,* Nagra, Wettingen, Switzerland. Available at nagra.ch.

Kaehr, D., Stockhecke, M., & Weber, H.P. (2023). TBO Bachs-1-1: Data Report, Dossier II: Core photography. *Nagra Arbeitsbericht, NAB 22-04,* Nagra, Wettingen, Switzerland. Available at nagra.ch.

Kaehr, D., & Gysi, M. (2023). TBO Rheinau-1-1: Data Report, Dossier II: Core photography. *Nagra Arbeitsbericht, NAB 22-03,* Nagra, Wettingen, Switzerland. Available at nagra.ch.

Kneuker, T., & Furche, M. (2021). Capturing the structural and compositional variability of Opalinus Clay: Constraints from multidisciplinary investigations of Mont Terri drill cores (Switzerland). *Environmental Earth Sciences, 80*, 421. https://doi.org/10.1007/s12665-021-09708-1

Korte, C., Hesselbo, S. P., Ullmann, C. V., Dietl, G., Ruhl, M., Schweigert, G., & Thibault, N. (2015). Jurassic climate mode governed by ocean gateway. *Nature Communications, 6*, 10015. https://doi.org/10.1038/ncomms10015

Kremer, K., Wirth, S. B., Reusch, A., Fäh, D., Bellwald, B., Anselmetti, F. S., Girardclos, S., & Strasser, M. (2017). Lake-sediment based paleoseismology: Limitations and perspectives from the Swiss Alps. *Quaternary Science Reviews, 168*, 1–18. https://doi.org/10.1016/j.quascirev.2017.04.026

Lauper, B. (2021). Characterisation of lithological heterogeneity within the Opalinus Clay and at its upper lithostratigraphic boundary (N Switzerland). *PhD Thesis.* University of Fribourg, Fribourg, Switzerland

Lauper, B., Deplazes, G., Vogel, H., Jaeggi, D., Wohlwend, S., Ariztegui, D., & Foubert, A. (2021a). Geochemical fingerprinting of key lithologies and depositional processes across the upper boundary of the Opalinus Clay (Aalenian, Middle Jurassic, northern Switzerland). *The Depositional Record, 7*, 25–51. https://doi.org/10.1002/dep2.126

Lauper, B., Jaeggi, D., Deplazes, G., & Foubert, A. (2018). Multi-proxy facies analysis of the Opalinus Clay and depositional implications (Mont Terri rock laboratory, Switzerland). *Swiss Journal of Geosciences, 111*, 383–398. https://doi.org/10.1007/s00015-018-0303-x

Lauper, B., Zimmerli, G. N., Jaeggi, D., Deplazes, G., Wohlwend, S., Rempfer, J., & Foubert, A. (2021b). Quantification of lithological heterogeneity within Opalinus Clay: Toward a uniform subfacies classification scheme using a novel automated core image recognition tool. *Frontiers in Earth Science, 9*, 645596. https://doi.org/10.3389/feart.2021.645596

Lazar, O. R., Bohacs, K. M., Macquaker, J. H. S., Schieber, J., & Demko, T. M. (2015). Capturing key attributes of fine-grained sedimentary rocks in outcrops, cores, and thin sections: Nomenclature and description guidelines. *Journal of Sedimentary Research, 85*, 230–246. https://doi.org/10.2110/jsr.2015.11

Lerouge, C., Grangeon, S., Claret, F., Gaucher, E., Blanc, P., Guerrot, C., Flehoc, C., Wille, G., & Mazurek, M. (2014). Mineralogical and isotopic record of diagenesis from the Opalinus Clay Formation at Benken, Switzerland: Implications for the modeling of pore-water chemistry in a clay formation. *Clays and Clay Minerals, 62*(4), 286–312. https://doi.org/10.1346/CCMN.2014.0620404

Leu, K., Zeeden, C., Mann, T., Erbacher, J., Bornemann, A., & Wonik, T. (2023). Cyclostratigraphy of the Lower Aalenian Opalinuston Formation in the Swabian Alb deduced from downhole logging data. *Zeitschrift Der Deutschen Gesellschaft Für Geowissenschaften, 174*, 53–67. https://doi.org/10.1127/zdgg/2023/0373

Lewis, K. B. (1971). Slumping on a continental slope inclined at 1°–4°. *Sedimentology, 16*, 97–110. https://doi.org/10.1111/j.1365-3091.1971.tb00221.x

Löwemark, L., Chen, H.-F., Yang, T.-N., Kylander, M., Yu, E.-F., Hsu, Y.-W., Lee, T.-Q., Song, S.-R., & Jarvis, S. (2011). Normalizing XRF-scanner data: a cautionary note on the interpretation of high-resolution records from organic-rich lakes. *Journal of Asian Earth Sciences, 40*, 1250–1256. https://doi.org/10.1016/j.jseaes.2010.06.002

Mäder, U., Aschwanden, L., Camesi, L., Gimmi, T., Jenni, A., Kiczka, M., Mazurek, M., Rufer, D., Waber, H.N., Wersin, P., Zwahlen, C., & Traber, D. (2021). TBO Marthalen-1-1: Data Report, Dossier VIII: Rock properties, porewater characterisation and natural tracer profiles. *Nagra Arbeitsbericht, NAB 21-20,* Nagra, Wettingen, Switzerland. Available at nagra.ch

Magalhães, A. J. C., Raja Gabaglia, G. P., Fragoso, D. G. C., Bento Freire, E., Lykawka, R., Arregui, C. D., Silveira, M. M. L., Carpio, K. M. T., De Gasperi, A., Pedrinha, S., Artagão, V. M., Terra, G. J. S., Bunevich, R. B., Roemers-Oliveira, E., Gomes, J. P., Hernández, J. I., Hernández, R. M., & Bruhn, C. H. L. (2020). High-resolution sequence stratigraphy applied to reservoir zonation and characterisation, and its impact on production performance—Shallow marine, fluvial downstream, and lacustrine carbonate settings. *Earth-Science Reviews, 210*, 103325. https://www.sciencedirect.com/science/article/pii/S0012825220303718

Marnat, S., & Becker, J.K. (2020). Petrophysical log analyses of deep and shallow boreholes: methodology report. *Nagra Arbeitsbericht, NAB 20-30,* Nagra, Wettingen, Switzerland. Available at nagra.ch.

Marnat, S., & Becker, J.K. (2021c). TBO Trüllikon-1-1: Data Report, Dossier X: Petrophysical log analysis. *Nagra Arbeitsbericht, NAB 20-09,* Nagra, Wettingen, Switzerland. Available at nagra.ch.

Marnat, S., & Becker, J.K. (2021b). TBO Marthalen-1-1: Data Report, Dossier X: Petrophysical log analysis. *Nagra Arbeitsbericht, NAB 21-20,* Nagra, Wettingen, Switzerland. Available at nagra.ch.

Marnat, S., & Becker, J.K. (2021a). TBO Bülach-1-1: Data Report, Dossier X: Petrophysical log analysis. *Nagra Arbeitsbericht, NAB 20-08,* Nagra, Wettingen, Switzerland. Available at nagra.ch.

Marnat, S., & Becker, J.K. (2022c). TBO Stadel-2-1: Data Report, Dossier X: Petrophysical log analysis. *Nagra Arbeitsbericht, NAB 22-02,* Nagra, Wettingen, Switzerland. Available at nagra.ch.

Marnat, S., & Becker, J.K. (2022d). TBO Stadel-3-1: Data Report, Dossier X: Petrophysical log analysis. *Nagra Arbeitsbericht, NAB 22-01,* Nagra, Wettingen, Switzerland. Available at nagra.ch.

Marnat, S., & Becker, J.K. (2022a). TBO Bözberg-1-1: Data Report, Dossier X: Petrophysical log analysis. *Nagra Arbeitsbericht, NAB 21-21,* Nagra, Wettingen, Switzerland. Available at nagra.ch.

Marnat, S., & Becker, J.K. (2022b). TBO Bözberg-2-1: Data Report, Dossier X: Petrophysical log analysis. *Nagra Arbeitsbericht, NAB 21-22,* Nagra, Wettingen, Switzerland. Available at nagra.ch.

Marnat, S., & Becker, J.K. (2023b). TBO Rheinau-1-1: Data Report, Dossier X: Petrophysical log analysis. *Nagra Arbeitsbericht, NAB 22-03,* Nagra, Wettingen, Switzerland. Available at nagra.ch.

Marnat, S., & Becker, J.K. (2023a). TBO Bachs-1-1: Data Report, Dossier X: Petrophysical log analysis. *Nagra Arbeitsbericht, NAB 22-04,* Nagra, Wettingen, Switzerland. Available at nagra.ch.

Matter, A., Peters, T., Isenschmid, C., Bläsi, H.R., & Ziegler, H.J. (1987). Sondierbohrung Riniken - Geologie. *Nagra Technischer Bericht, NTB 86-02,* Nagra, Wettingen, Switzerland. Available at nagra.ch.

Matter, A., Peters, T., Bläsi, H.R., Meyer, J., Ischi, H., & Meyer, C. (1988). Sondierbohrung Weiach—Geologie. *Nagra Technischer Bericht, NTB 86-01,* Nagra, Wettingen, Switzerland. Available at nagra.ch.

Mazurek, M., & Aschwanden, L. (2020). Multi-scale petrographic and structural characterisation of the Opalinus Clay. *Nagra Arbeitsbericht, NAB 19-44*, Nagra, Wettingen, Switzerland. Available at nagra.ch.

Mazurek, M., Aschwanden, L., Camesi, L., Gimmi, T., Jenni, A., Kiczka, M., Mäder, U., Rufer, D., Waber, H.N., Wanner, P., Wersin, P., & Traber, D. (2021). TBO Bülach-1-1: Data Report, Dossier VIII: Rock properties, porewater characterisation and natural tracer profiles. *Nagra Arbeitsbericht, NAB 20-08,* Nagra, Wettingen, Switzerland. Available at nagra.ch.

Mazurek, M., Gimmi, T., Zwahlen, C., Aschwanden, L., Gaucher, E. C., Kiczka, M., Rufer, D., Wersin, P., Marques Fernandes, M., Glaus, M. A., Van Loon, L. R., Traber, D., Schnellmann, M., & Vietor, T. (2023). Swiss deep drilling campaign 2019–2022: Geological overview and rock properties with focus on porosity and pore-space architecture. *Applied Geochemistry, 159,* 105839. https://doi.org/10.1016/j.apgeochem.2023.105839

Miall, A. D. (2010). *The geology of stratigraphic sequences* (2nd ed.). Springer

Mitchum, R. M., & Van Wagoner, J. C. (1991). High-frequency sequences and their stacking patterns: Sequence-stratigraphic evidence of high-frequency eustatic cycles. *Sedimentary Geology, 70*, 131–160. https://www.sciencedirect.com/science/article/abs/pii/0037073891901395

Molenaar, A., Van Daele, M., Huang, J.-J.S., Strasser, M., De Batist, M., Pino, M., Urrutia, R., & Moernaut, J. (2022). Disentangling factors controlling earthquake-triggered soft-sediment deformation in lakes. *Sedimentary Geology, 438*, 106200. https://doi.org/10.1016/j.sedgeo.2022.106200

Montenat, C., Barrier, P., Ott d'Estevou, P., & Hibsch, C. (2007). Seismites: An attempt at critical analysis and classification. *Sedimentary Geology, 196*, 5–30. https://doi.org/10.1016/j.sedgeo.2006.08.004

Morettini, E., Santantonio, M., Bartolini, A., Cecca, F., Baumgartner, P. O., & Hunziker, J. C. (2002). Carbon isotope stratigraphy and carbonate production during the Early-Middle Jurassic: Examples from the Umbria–Marche–Sabina Apennines (central Italy). *Palaeogeography, Palaeoclimatology, Palaeoecology, 184*, 251–273. https://doi.org/10.1016/S0031-0182(02)00258-4

Naef, H., Büchi, M., Bläsi, H.R., Deplazes, G., & Gysi, M. (2019). Lithology manual—lithological description of drill cores and cuttings in northern Switzerland. *Nagra Arbeitsbericht, NAB 19-11,* Nagra, Wettingen, Switzerland. Available at nagra.ch.

Nagra. (2001). Sondierbohrung Benken—Untersuchungsbericht. *Nagra Technischer Bericht, NTB 00-01,* Nagra, Wettingen, Switzerland. Available at nagra.ch.

Nagra. (2002). Projekt Opalinuston: Synthese der geowissenschaftlichen Untersuchungsergebnisse. Entsorgungsnachweis für abgebrannte Brennelemente, verglaste hochaktive sowie langlebige mittelaktive Abfälle. *Nagra Technischer Bericht, NTB 02-03*, Nagra, Wettingen, Switzerland. Available at nagra.ch.

Nagra. (2014b). SGT Etappe 2: Vorschlag weiter zu untersuchender geologischer Standortgebiete mit zugehörigen Standortarealen für die Oberflächenanlage: Geologische Grundlagen, Dossier II: Sedimentologische und tektonische Verhältnisse. *Nagra Technischer Bericht, NTB 14-02,* Nagra, Wettingen, Switzerland. Available at nagra.ch.

Nagra. (2014a). SGT Etappe 2: Vorschlag weiter zu untersuchender geologischer Standortgebiete mit zugehörigen Standortarealen für die Oberflächenanlage: Geologische Grundlagen, Dossier I: Einleitung und Zusammenfassung. *Nagra Technischer Bericht, NTB 14-02*, Nagra, Wettingen, Switzerland. Available at nagra.ch.

Nigg, V., Bacigaluppi, P., Vetsch, D. F., Vogel, H., Kremer, K., & Anselmetti, F. S. (2021). Shallow-water tsunami deposits: evidence from sediment cores and numerical wave propagation of the 1601 CE Lake Lucerne event. *Geochemistry, Geophysics, Geosystems, 22*, e2021GC009753. https://doi.org/10.1029/2021GC009753

Nikitenko, B., Shurygin, B., & Mickey, M. (2008). High resolution stratigraphy of the Lower Jurassic and Aalenian of Arctic regions as the basis for detailed palaeobiogeographic reconstructions. *Norwegian Journal of Geology, 88*, 267–277.

Oksanen, J., Blanchet, F.G., Friendly, M., Kindt, R., Legendre, P., McGlinn, D., Minchin, P.R., O'Hara, R.B., Simpson, G.L., Solymos, P., Henry, M., Stevens, H., Szoecs, E., & Wagner, H. (2016). Vegan: community ecology package, R package version. *R Foundation for Statistical Computing*, Vienna, Austria.

Ollier, C. D. (1969). *Weathering. Geomorphology Texts* (p. 304). Oliver and Boyd.

Owen, G., & Moretti, M. (2011). Identifying triggers for liquefaction-induced soft-sediment deformation in sands. *Sedimentary Geology, 235*, 141–147. https://doi.org/10.1016/j.sedgeo.2010.10.003

Paz, M., Buatois, L. A., Mángano, M. G., Desjardins, P. R., Notta, R., Tomassini, F. G., Carmona, N. B., & Minisini, D. (2022). Organic-rich, fine-grained contourites in an epicontinental basin: The Upper Jurassic-Lower Cretaceous Vaca Muerta Formation, Argentina. *Marine and Petroleum Geology, 142*, 105757. https://doi.org/10.1016/j.marpetgeo.2022.105757

Pearson, F.J., Arcos, D., Bath, A., Boisson, J.-Y., Fernández, A.M., Gäbler, H.-E., Gaucher, E., Gautschi, A., Griffault, L., Hernán, P., & Waber, H.N. (2003). Mont Terri project - geochemistry of water in the Opalinus Clay Formation at the Mont Terri rock laboratory. *Reports of the Federal Office for Water and Geology (FOWG), Geology Series, No. 5*. Bern, Switzerland

Pieńkowski, G., Schudack, M.E., Bosák, P., Enay, R., Feldman-Olszewska, A., Golonka, J., Gutowski, J., Herngreen, G.F.W., Jordan, P., Krobicki, M., Lathuiliere, B., Leinfelder, R.R., Michalík, J., Mönnig, E., Noe-Nygaard, N., Pálfy, J., Pint, A., Rasser, M.W., Reisdorf, A.G., Schmid, D.U., Schweigert, G., Surlyk, F., Wetzel, A., & Wong, T.E. (2008). Jurassic. In T. McCann (Ed.), *The Geology of Central Europe, Volume 2: Mesozoic and Cenozoic*. London: The Geological Society. https://doi.org/10.1144/CEV2P.2

Pieńkowski, G., Uchman, A., Ninard, K., & Hesselbo, S. P. (2021). Ichnology, sedimentology, and orbital cycles in the hemipelagic Early Jurassic Laurasian Seaway (Pliensbachian, Cardigan Bay Basin, UK). *Global and Planetary Change, 207*, 103648. https://doi.org/10.1016/j.gloplacha.2021.103648

Price, G. D. (2010). Carbon-isotope stratigraphy and temperature change during the Early-Middle Jurassic (Toarcian–Aalenian), Raasay, Scotland, UK. *Palaeogeography, Palaeoclimatology, Palaeoecology, 285*, 255–263. https://doi.org/10.1016/j.palaeo.2009.11.018

R Core Team. (2022). R: A language and environment for statistical computing. *R Foundation for Statistical Computing*, Vienna, Austria. https://www.R-project.org/

Reading, H. G. (1996). *Sedimentary environments: processes, facies and stratigraphy* (3rd ed.). Blackwell Science

Rebesco, M., Hernández-Molina, F. J., Van Rooij, D., & Wåhlin, A. (2014). Contourites and associated sediments controlled by deep-water circulation processes: State-of-the-art and future considerations. *Marine Geology, 352*, 111–154. https://doi.org/10.1016/j.margeo.2014.03.011

Reisdorf, A. G., & Wetzel, A. (2018). Evidence for synsedimentary differential tectonic movements in a low-subsidence setting: Early Jurassic in northwestern Switzerland. *Swiss Journal of Geosciences, 111*, 417–444. https://doi.org/10.1007/s00015-018-0318-3

Reisdorf, A. G., Wetzel, A., Schlatter, R., & Jordan, P. (2011). The Staffelegg Formation: A new stratigraphic scheme for the Early Jurassic of northern Switzerland. *Swiss Journal of Geosciences, 104*, 97–146. https://doi.org/10.1007/s00015-011-0057-1

Rogov, M. A., & Zakharov, V. A. (2010). Jurassic and Lower Cretaceous glendonite occurrences and their implication for arctic paleoclimate reconstructions and stratigraphy. *Earth Science Frontiers, 17*(Special Issue), 345–347

Rothwell, R. G., & Croudace, I. W. (2015). Chapter 2: Twenty years of XRF core scanning marine sediments: What do geochemical proxies tell us? In I. W. Croudace & R. G. Rothwell (Eds.), *Micro XRF studies of sediment cores, developments in paleoenvironmental research* (Vol. 17, pp. 25–102). Dordrecht: Springer. https://doi.org/10.1007/978-94-017-9849-5_2

Ruffell, A., McKinley, J. M., & Worden, R. H. (2002). Comparison of clay mineral stratigraphy to other proxy palaeoclimate indicators in the Mesozoic of NW Europe. *Philosophical Transactions of the Royal Society of London Series a: Mathematical, Physical and Engineering Sciences, 360*, 675–693. https://doi.org/10.1098/rsta.2001.0961

Sandoval, J., O'Dogherty, L., Aguado, R., Bartolini, A., Bruchez, S., & Bill, M. (2008). Aalenian carbon-isotope stratigraphy: Calibration with ammonite, radiolarian and nannofossil events in the Western Tethys. *Palaeogeography, Palaeoclimatology, Palaeoecology, 267*, 115–137. https://doi.org/10.1016/j.palaeo.2008.06.013

Scarselli, N., McClay, K., & Elders, C. (2019). Seismic examples of composite slope failures (offshore north west shelf, Australia). In K. Ogata, A. Festa, & G. A. Pini (Eds.), *Submarine landslides: Subaqueous mass transport deposits from outcrops to seismic profiles* (pp. 261–276). Wiley. https://doi.org/10.1002/9781119500513.ch16

Schieber, J. (2016). Mud re-distribution in epicontinental basins—Exploring likely processes. *Marine and Petroleum Geology, 71*, 119–133. https://doi.org/10.1016/j.marpetgeo.2015.12.014

Schnellmann, M., Anselmetti, F. S., Giardini, D., & McKenzie, J. A. (2005). Mass movement-induced fold-and-thrust belt structures in unconsolidated sediments in Lake Lucerne (Switzerland). *Sedimentology, 52*, 271–289. https://doi.org/10.1111/j.1365-3091.2004.00694.x

Schnellmann, M., Anselmetti, F. S., Giardini, D., & McKenzie, J. A. (2006). 15,000 years of mass-movement history in Lake Lucerne: Implications for seismic and tsunami hazards. *Eclogae Geologicae Helvetiae, 99*, 409–428. https://doi.org/10.1007/s00015-006-1196-7

Schnellmann, M., Anselmetti, F. S., Giardini, D., McKenzie, J. A., & Ward, S. N. (2002). Prehistoric earthquake history revealed by lacustrine slump deposits. *Geology, 30*(12), 1131–1134. https://doi.org/10.1130/0091-7613(2002)030%3c1131:PEHRBL%3e2.0.CO;2

Schürch, P., Jordan, P., Schwarz, M., Naef, H., Felber, R., Ibele, T., & Gysi, M. (2022). TBO Stadel-3-1: Data Report, Dossier III: Lithostratigraphy. *Nagra Arbeitsbericht, NAB 22-01,* Nagra, Wettingen, Switzerland. Available at nagra.ch

Schwarz, M., Jordan, P., Schürch, P., Naef, H., Ibele, T., Felber, R., & Gysi, M. (2021). TBO Trüllikon-1-1: Data Report, Dossier III: Lithostratigraphy. *Nagra Arbeitsbericht, NAB 20-09,* Nagra, Wettingen, Switzerland. Available at nagra.ch

Schwarz, M., Schürch, P., Naef, H., Jordan, P., Felber, R., Ibele, T., & Gysi, M. (2022). TBO Bözberg-1-1: Data Report, Dossier III: Lithostratigraphy. *Nagra Arbeitsbericht, NAB 21-21,* Nagra, Wettingen, Switzerland. Available at nagra.ch

Schwarz, M., Schürch, P., Jordan, P., Naef, H., Felber, R., Ibele, T., & Casanova, F. (2023). TBO Rheinau-1-1: Data Report, Dossier III: Lithostratigraphy. *Nagra Arbeitsbericht, NAB 22-03,* Nagra, Wettingen, Switzerland. Available at nagra.ch.

Shanmugam, G. (2017). Contourites: Physical oceanography, process sedimentology, and petroleum geology. *Petroleum Exploration and Development, 44*(2), 183–216. https://doi.org/10.1016/S1876-3804(17)30023-X

Shanmugam, G. (2019). Slides, slumps, debris flows, turbidity currents, hyperpycnal flows, and bottom currents. *Encyclopedia of Ocean Sciences* (3rd ed., pp. 228–257). Elsevier. https://doi.org/10.1016/B978-0-12-409548-9.10884-X

Sibson, R. (1972). Order invariant methods for data analysis. *Journal of the Royal Statistical Society, Series B, 34*(3), 311–349

Stow, D., & Smillie, Z. (2020). Distinguishing between deep-water sediment facies: Turbidites, contourites and hemipelagites. *Geosciences, 10*, 68. https://doi.org/10.3390/geosciences10020068

Strachan, L. J. (2002). Slump-initiated and controlled syndepositional sandstone remobilization: An example from the Namurian of County Clare, Ireland. *Sedimentology, 49*, 25–41. https://doi.org/10.1046/j.1365-3091.2002.00430.x

Strupler, M., Hilbe, M., Kremer, K., Daciu, L., Anselmetti, F. S., Strasser, M., & Wiemer, S. (2018). Subaqueous landslide-triggered tsunami hazard for Lake Zurich, Switzerland. *Swiss Journal of Geosciences, 111*, 353–371. https://doi.org/10.1007/s00015-018-0308-5

Thiry, M. (2000). Palaeoclimatic interpretation of clay minerals in marine deposits: An outlook from the continental origin. *Earth-Science Reviews, 49*, 201–221. https://doi.org/10.1016/S0012-8252(99)00054-9

Thury, M., & Bossart, P. (1999). The Mont Terri rock laboratory, a new international research project in a Mesozoic shale formation, in Switzerland. *Engineering Geology, 52*, 347–359. https://doi.org/10.1016/S0013-7952(99)00015-0

Underhill, J.R., & Partington, M.A. (1993). Jurassic thermal doming and deflation in the North Sea: implications of the sequence stratigraphic evidence. *Petroleum Geology of Northwest Europe: Proceedings of the 4th Conference*, 337–345. https://doi.org/10.1144/0040337

Voigt, E. (1968). Über Hiatus-Konkretionen (dargestellt an Beispielen aus dem Lias). *Geologische Rundschau, 58*, 281–296

Waber, H.N., & Rufer, D. (2017). Porewater geochemistry, method comparison and Opalinus Clay—Passwang Formation interface study at the Mont Terri URL. *NWMO Technical Reports, TR-2017-10*, Nuclear waste management organization, Toronto, Canada

Waber, H.N. (2020). SGT-E3 deep drilling campaign (TBO): experiment procedures and analytical methods at RWI, University of Bern (Version 1.0, April 2020). *Nagra Arbeitsbericht, NAB 20-13,* Nagra, Wettingen, Switzerland. Available at nagra.ch

Wersin, P., Aschwanden, L., Camesi, L., Gaucher, E.C., Gimmi, T., Jenni, A., Kiczka, M., Mäder, U., Mazurek, M., Rufer, D., Waber, H.N., Zwahlen, C., & Traber, D. (2022). TBO Bözberg-1-1: Data Report, Dossier VIII: Rock properties, porewater characterisation and natural tracer profiles. *Nagra Arbeitsbericht, NAB 21-21,* Nagra, Wettingen, Switzerland. Available at nagra.ch

Wetzel, A., Allenbach, R., & Allia, V. (2003). Reactivated basement structures affecting the sedimentary facies in a tectonically "quiescent" epicontinental basin: An example from NW Switzerland. *Sedimentary Geology, 157*, 153–172. https://doi.org/10.1016/S0037-0738(02)00230-0

Wetzel, A., & Allia, V. (1996). Der Ablagerungsraum des Opalinustons-eine sedimentologische Analyse. *Geologisches Landesamt Baden-Württemberg, Information, 8*, 20–24

Wetzel, A., & Allia, V. (2000). The significance of hiatus beds in shallow-water mudstones: An example from the Middle Jurassic of Switzerland. *Journal of Sedimentary Research, 70*(1), 170–180. https://doi.org/10.1306/2DC40908-0E47-11D7-8643000102C1865D

Wetzel, A., & Allia, V. (2003). Der Opalinuston in der Nordschweiz: Lithologie und Ablagerungsgeschichte. *Eclogae Geologicae Helvetiae, 96*, 451–469. https://doi.org/10.5169/seals-169032

Wetzel, A., & Meyer, C. A. (2006). The dangers of high-rise living on a muddy seafloor: An example of crinoids from shallow-water mudstones (Aalenian, northern Switzerland). *Palaios, 21*, 155–167. https://doi.org/10.2110/palo.2005.p05-132

Wetzel, A., & Unverricht, D. (2013). A muddy megaturbidite in the deep central South China Sea deposited ~ 350 yrs BP. *Marine Geology, 346*, 91–100. https://doi.org/10.1016/j.margeo.2013.08.010

Wetzel, A., Werner, F., & Stow, D. A. V. (2008). Chapter 11: Bioturbation and biogenic sedimentary structures in contourites. In M. Rebesco & A. Camerlenghi (Eds.), *Contourites. Developments in sedimentology* (Vol. 60, pp. 183–202). Amsterdam: Elsevier. https://doi.org/10.1016/S0070-4571(08)10011-5

Wickham, H., François, R., Henry, L., & Müller, K. (2022). dplyr: a grammar of data manipulation. https://dplyr.tidyverse.org, https://github.com/tidyverse/dplyr

Wohlwend, S., Bläsi, H.R., Feist-Burkhardt, S., Hostettler, B., Menkveld-Gfeller, U., Dietze, V., & Deplazes, G. (2019). Die Passwang-Formation im östlichen Falten- und Tafeljura: Fasiswald (SO)—Unt. Hauenstein (SO)–Wasserflue (AG)–Thalheim (AG)–Frickberg (AG)–Cheisacher (AG)–Böttstein (AG)–Tegerfelden (AG)–Acheberg (AG). *Nagra Arbeitsbericht, NAB 18-11,* Nagra, Wettingen, Switzerland. Available at nagra.ch

Wohlwend, S., Bläsi, H.R., Feist-Burkhardt, S., Hostettler, B., Menkveld-Gfeller, U., Dietze, V., & Deplazes, G. (2021c). TBO Trüllikon-1-1: Data Report, Dossier IV: Microfacies, bio- and chemostratigraphic analysis. *Nagra Arbeitsbericht, NAB 20-09,* Nagra, Wettingen, Switzerland. Available at nagra.ch

Wohlwend, S., Bläsi, H.R., Feist-Burkhardt, S., Hostettler, B., Menkveld-Gfeller, U., Dietze, V., & Deplazes, G. (2021b). TBO Marthalen-1-1: Data Report, Dossier IV: Microfacies, bio- and chemostratigraphic analysis. *Nagra Arbeitsbericht, NAB 21-20,* Nagra, Wettingen, Switzerland. Available at nagra.ch

Wohlwend, S., Bläsi, H.R., Feist-Burkhardt, S., Hostettler, B., Menkveld-Gfeller, U., Dietze, V., & Deplazes, G. (2021a). TBO Bülach-1-1: Data Report, Dossier IV: Microfacies, bio- and chemostratigraphic analysis. *Nagra Arbeitsbericht, NAB 20-08,* Nagra, Wettingen, Switzerland. Available at nagra.ch

Wohlwend, S., Bläsi, H.R., Feist-Burkhardt, S., Hostettler, B., Menkveld-Gfeller, U., Dietze, V., & Deplazes, G. (2022c). TBO Stadel-2-1: Data Report, Dossier IV: Microfacies, bio- and chemostratigraphic analysis. *Nagra Arbeitsbericht, NAB 22-02,* Nagra, Wettingen, Switzerland. Available at nagra.ch

Wohlwend, S., Bläsi, H.R., Feist-Burkhardt, S., Hostettler, B., Menkveld-Gfeller, U., Dietze, V., & Deplazes, G. (2022d). TBO Stadel-3-1: Data Report, Dossier IV: Microfacies, bio- and chemostratigraphic analysis. *Nagra Arbeitsbericht, NAB 22-01,* Nagra, Wettingen, Switzerland. Available at nagra.ch

Wohlwend, S., Bläsi, H.R., Feist-Burkhardt, S., Hostettler, B., Menkveld-Gfeller, U., Dietze, V., & Deplazes, G. (2022a). TBO Bözberg-1-1: Data Report, Dossier IV: Microfacies, bio- and chemostratigraphic analysis. *Nagra Arbeitsbericht, NAB 21-21,* Nagra, Wettingen, Switzerland. Available at nagra.ch

Wohlwend, S., Bläsi, H.R., Feist-Burkhardt, S., Hostettler, B., Menkveld-Gfeller, U., Dietze, V., & Deplazes, G. (2022b). TBO Bözberg-2-1: Data Report, Dossier IV: Microfacies, bio- and chemostratigraphic analysis. *Nagra Arbeitsbericht, NAB 21-22,* Nagra, Wettingen, Switzerland. Available at nagra.ch

Wohlwend, S., Bläsi, H.R., Feist-Burkhardt, S., Hostettler, B., Menkveld-Gfeller, U., Dietze, V., & Deplazes, G. (2023b). TBO Rheinau-1-1: Data Report, Dossier IV: Microfacies, bio- and chemostratigraphic analysis. *Nagra Arbeitsbericht, NAB 22-03,* Nagra, Wettingen, Switzerland. Available at nagra.ch

Wohlwend, S., Bläsi, H.R., Feist-Burkhardt, S., Hostettler, B., Menkveld-Gfeller, U., Dietze, V., & Deplazes, G. (2023a). TBO Bachs-1-1: Data Report, Dossier IV: Microfacies, bio- and chemostratigraphic analysis. *Nagra Arbeitsbericht, NAB 22-04,* Nagra, Wettingen, Switzerland. Available at nagra.ch

Wohlwend, S., Hostettler, B., Menkveld-Gfeller, U., Feist-Burkhardt, S., Bläsi, H., Zimmerli, G. N., Dietze, V., Bernasconi, S. M., & Deplazes, G. (2024). High-resolution bio- and chemostratigraphy of the Toarcian to Aalenian of Northern Switzerland with a focus on the Opalinus Clay. *Newsletters on Stratigraphy*. https://doi.org/10.1127/nos/2024/0823

Zimmermann, J., Franz, M., Heunisch, C., Luppold, F. W., Mönnig, E., & Wolfgramm, M. (2015). Sequence stratigraphic framework of the Lower and Middle Jurassic in the North German Basin: Epicontinental sequences controlled by boreal cycles. *Palaeogeography, Palaeoclimatology, Palaeoecology, 440*, 395–416. https://doi.org/10.1016/j.palaeo.2015.08.045

Zimmermann, J., Franz, M., Schaller, A., & Wolfgramm, M. (2018). The Toarcian-Bajocian deltaic system in the North German Basin: Subsurface mapping of ancient deltas-morphology, evolution and controls. *Sedimentology, 65*, 897–930. https://doi.org/10.1111/sed.12410

Zwahlen, C., Aschwanden, L., Gaucher, E., Gimmi, T., Jenni, A., Kiczka, M., Mäder, U., Mazurek, M., Ross, D., Rufer, D., Waber, H.N., Wersin, P., & Traber, D. (2022). TBO Stadel-2-1: Data Report, Dossier VIII: Rock properties, porewater characterisation and natural tracer profiles. *Nagra Arbeitsbericht, NAB 22-02,* Nagra, Wettingen, Switzerland. Available at nagra.ch

Publisher's Note

Springer Nature remains neutral with regard to jurisdictional claims in published maps and institutional affiliations.